Delft University of Technology

Preliminary Room and Pillar Mine Design in Fractured Limestone

A Comparative Analysis of Empirical and Numerical Methods

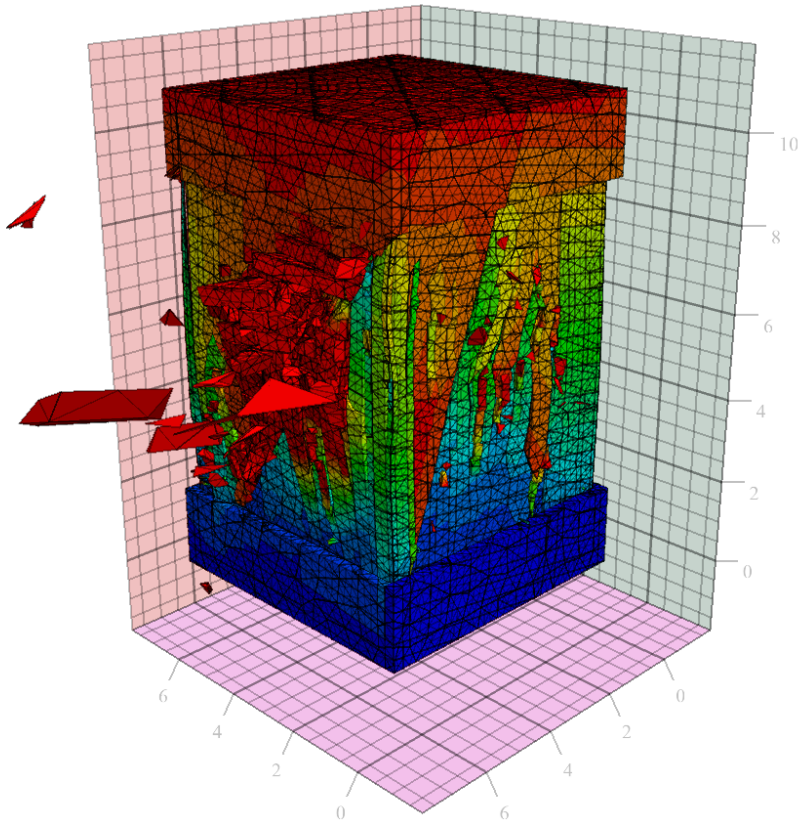

Author
H.J.P. Oostman

Supervisor
Dr. P.B.R. Bruna
Dr. Ir. D.J.M. Ngan-Tillard

October 11, 2024

Preface

Throughout this research, I gained a much better understanding of numerical modelling. Working extensively with 3DEC was incredibly challenging but also exciting. Much of the modelling process involved figuring out the code and the underlying mechanics of 3DEC on my own, which required a lot of trial and error. This hands-on experience revealed how many different parameters can influence a model, adding layers of complexity to the analysis. One of the main challenges was the time it took to understand the code and the effect of various parameters. Unfortunately, I feel that the substantial time investment involved in this learning process is not fully reflected in the research. I chose not to include all of these findings because including them would have required a separate sensitivity analysis for each of them, which was not possible with the time available. In hindsight, it would have been better to focus on one of these parameter sensitivity analyses and use fictive data to investigate its effect more efficiently. Instead, I planned to determine the pillar strength and roof stability with various rock bolting patterns and look at the deformation of an entire room and pillar mine with different excavation stages. This was found to be too ambitious, which was the reason the 3DEC modelling was scaled down to only the pillars. Despite these challenges, discovering how each parameter affects the model has been crucial in my learning process. I have developed a stronger ability to tackle complex problems by isolating key issues in the code and adjusting parameters accordingly. This experience has also deepened my understanding of the proper use of numerical models, what their strengths are and in which scenarios the empirical method is a more straightforward method to apply.

Summary

This research evaluates two methods for determining the optimal dimensions of a fictive room and pillar (R&P) mine at the Marche Les Dames (MLD) quarry in Belgium. The empirical method, including the Q-system and the R&P design guidelines from NIOSH (2011), is used to calculate roof spans and pillar dimensions. These calculated pillar dimensions are then modelled using the Distinct Element Method (DEM) software, 3DEC, and the results will be compared with those of the empirical method. The pillar is modelled using a Bounded Block Model (BBM) approach and integrating a Discrete Fracture Network (DFN) to account for the fractured rock mass. The empirical method offered straightforward results and is well-suited for preliminary mine design. However, it is unable to incorporate the heterogeneity of the rock mass, providing only a limited understanding of its behaviour. In contrast, the numerical method can incorporate this heterogeneity, offering a more detailed analysis. However, collecting all necessary parameters is challenging, and calibration and validation are required—something that was not fully achieved in this research.

The study found that the numerical model produced unrealistic results when modelling stress-controlled failure in the pillars at MLD. The pillar strength was much higher than expected. This was attributed to the calibration of the intact rock strength using a UCS sample, which did not account for weaknesses in the intact rock. In contrast, when the failure was structurally controlled and the model did not require the BBM approach, the results were much more realistic, with significantly lower computational time. Still, it is recommended to use the numerical model primarily to investigate the impact of specific features such as karst voids and dissolution joints, which the empirical method cannot incorporate, rather than to determine overall mining dimensions.

Contents

1 Introduction

This research presents a fictive case for a potential expansion of the Marche Les Dames (MLD) quarry in Belgium, near Namêche. It is currently a large open-pit operation which could be extended using various mining methods, including open-pit, room and pillar (R&P), or sub-vertical stope mining. For this study, a hypothetical R&P expansion is chosen. The underground R&P mining method is one of the oldest methods for extracting ore from the subsurface and has its origin dating back to the 13^{th} century (Statham & Treharne, 1991). The method allows for the selective extraction of geological layers targeted for ore extraction while maintaining structural integrity by leaving support pillars. However, when the ore is close to the surface, open-pit mining boasts distinct advantages such as higher recovery, more cost-effectiveness, and a reduced risk in geotechnical challenges. There are some instances when, over time, a transition from open pit to underground R&P mining is required. For example, if the ore body or targeted geological layer is inclined, more overburden has to be excavated over time to extract the valuable material. This increases the cost and makes transitioning to underground mining favourable. Environmental factors also play an important role, while open pit mining can impact ecosystems by removing large quantities of overburden. And, with mining operations often close to populated areas, which is the case in most European countries, it is facing resistance from the local communities (Vasovic, 2024). Effects of the extraction of the ore, such as air pollution, noise, vibrations, visible impact, and the possibility of community displacement (e.g., the expansion of the massive coal mines in Germany), play a role in this resistance. Nevertheless, R&P operations are not free from consequences. Groundwater pollution, lowering of the groundwater table, vibrations caused by machines, and blasting all negatively affect the environment. And some of these consequences, with the added risk of subsidence, could also affect the local communities. This research will focus on the possible dimensions of an R&P operation, ensuring maximum recovery while maintaining a stable excavation. To achieve this goal, the study will apply the empirical method to determine the maximum roof span and minimum pillar width. Afterwards, the empirically determined pillar dimensions will be modelled using a numerical model, and the results will be compared.

The rock mass in the quarry consists of dolostone with near-horizontal bedding and two sub-vertical joint sets. These discontinuities affect the strength and behaviour of the rock mass, which limits the dimensions of the underground excavation. Incorporating the discontinuities in the empirical equation and numerical method is therefore crucial, where discontinuities represent any break in the continuum of the rock. Esterhuizen et al. (2019) showed that when the empirical equation does not include large angular discontinuities, it greatly overestimates the pillar strength. Large angular discontinuities have a dip higher than or equal to 30°and cross-cut the entire pillar. In their research, they determined with the use of FLAC3D that a pillar in a limestone mine in Pennsylvania experienced a stress of ±11.0 MPa at failure. They compared this with a pillar strength equation for limestone mines from Krauland and Soder (1987). This formula did not include discontinuities and predicted the pillar strength to be 57.8 MPa, while the pillar failed at a load of only 11.0 MPa. This difference highlights the need to integrate discontinuities into the empirical equations. The empirical methods used in this research are the Q-System (NGI, 2022) and the 'Pillar and Roof Span Design Guidelines for Underground Stone Mines' from the National Institute for Occupational Safety and Health (NIOSH, 2011) which will be referred to as the R&P design guidelines. Both methods allow for the integration of discontinuities.

The numerical model that will be used in this research is the distinct element method (DEM) software 3DEC. Two methods are available for modelling discontinuities within 3DEC. The first method involves creating planes with infinite length, often used to model persistent features like bedding planes. The second method generates a discrete fracture network (DFN) to model fractures within the rock mass. These fractures are created by stress, pressure, or temperature changes within the crust and include faults, joints, and fissures. A fracture network is a collection of fractures within a rock mass. DFNs use statistical methods to model fractures based on data like orientation, size, and density, often collected through field surveys or geophysical methods like ground penetrating radar (GPR). The data for DFN generation, Q-values, and joint properties are from Jolly (2024). The data on the intact rock properties is known for a selection of materials from laboratory tests performed at the Geoscience and Engineering Laboratory at the Delft University of Technology (Jolly & Oostman, 2023). The material tested consists of unweathered and weathered rock cores but excludes joint infill that can consist of clay or dolomitic sand.

To determine the maximum roof span of the underground excavation, a combination of the Q-system and R&P design guidelines is used. The Q-system allows for determining different roof spans for different support measures, which will be verified with the R&P design guidelines. The pillar strength equation from the R&P design guidelines is used to determine the pillar dimensions. These final pillar dimensions are modelled in 3DEC and loaded until failure. 3DEC allows us to investigate the failure mode, the effect of the different DFNs and the 3D effect of the discontinuities with respect to the pillar edges.

This research has two main objectives. The first is to determine possible R&P dimensions by applying the empirical method. The dimensions of the excavation include the maximum roof span and minimum pillar width. The second is modelling the pillar dimensions determined using the empirical method using 3DEC and loading the pillar until failure. Because of computational time, this will only happen for two of the four geotechnical units. The research aims to evaluate the differences in the results of the pillar strength between the two methods. Because there is no data on in situ pillar loading, it is difficult to determine which method produces the most realistic pillar strength. Therefore, the focus of comparing the two methods will be to see if both methods can account for the differences between the pillar strengths of different geotechnical units. In addition to the differences between geotechnical units, the variations within a single unit caused by the different generated DFNs within 3DEC will also be of interest. This comparison can not be made in the empirically determined dimensions whilst this does not incorporate a DFN.

2 State of the Art

This chapter provides an overview of the difference between empirical and numerical methods to determine underground mining dimensions. It will discuss the advantages and limitations of both methods. This chapter also explains why it is chosen to use a distinct element method (DEM) model compared to a finite element method (FEM) model to model the fractured rock mass in the Marche Les Dames (MLD) quarry. The fractures are incorporated by using a discrete fracture network (DFN), with the blocks between the fractures being modelled using a bounded block model (BBM) approach. Both of these features will also be elaborated on in this chapter.

Empirical equations, i.e., back-analysis of field performance, are often used in practice. The equations are relatively easy to use because of the low number of parameters (six parameters for both the Q-System and the pillar strength equation from NIOSH (2011)). However, their site-specific nature limits their use and tends to make them conservative. Another limitation is that the formulas do not allow for heterogeneity (e.g. different joint conditions for different joint sets) and time-dependent behaviour. The numerical method is currently widely used in rock mass applications because it allows the input of an anisotropic stress regime and heterogeneity of the rock mass properties into the model and can perform a time-dependent analysis. This gives the possibility to more accurately define pre-mining environments, estimate pillar load, model mining stages, analyse the entire mine as a composite structure, apply different failure criteria, and asses multiple failure modes (Galvin, 2016). However, difficulties arise when quantifying all the parameters in the model, which might limit the selection of the correct constitutive model. For example, a strain-softening model is more accurate than a purely elastic model but requires many more parameters like initial cohesion, friction angle, and tensile strength and their residual values. And when integrating complex geometries that require a dense mesh with a heterogeneous and fractured rock mass, the model can become computationally intensive. Another problem in numerical modelling is the validation of the model. This can be done by monitoring the deformation of the excavation and comparing it to the results of the numerical model. This comparison can help identify differences with the real world, and parameters that are not directly measured should be varied until the rock mass behaviour is similar. However, validation becomes problematic if such data is unavailable or the excavation is yet to be undertaken.

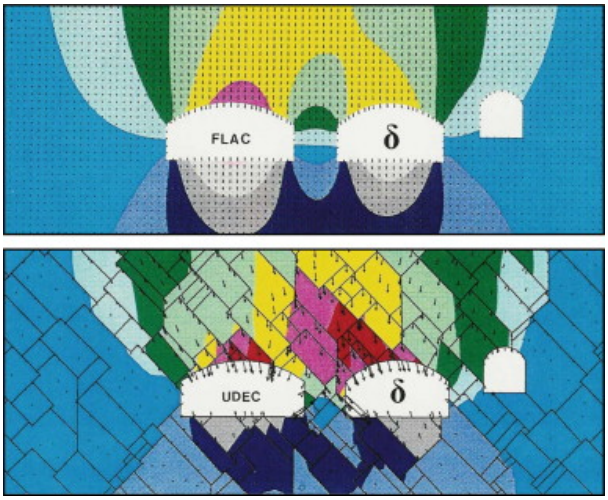

Figure 2.1: Comparison between continuum (FLAC) and discontinuum (UDEC) models showing the spoon-shaped failure in the continuum model and a more accurate representation of fractured rock mass behaviour in the discontinuum model (Barton, 2013)

The numerical model used in this research is a DEM model. It is a discontinuum model which is chosen over the more commonly used and computationally less intensive continuum model such as an FEM or finite difference (FDM) model. This discontinuum model is preferred because the fractured rock mass in a continuum model is often approximated by applying the Geological Strength Index (GSI) within the Generalized Hoek-Brown failure criterion (Tzalamarias et al., 2019; Sari, 2022). New developments in the continuum models allow for modelling fractures superimposed on the mesh with software such as RS3 from Rocscience. These updates are relatively recent, with DFN being integrated into RS3 as of August 2023 ("RS3 Program Updates," 2024). However, modelling a fractured rock mass using the GSI does not always provide realistic results. As Barton (2022) pointed out, by using this approach, plastic zones around tunnels are exaggerated, and predicted spoon-shaped failures are often not observed in the real world. Failure in competent jointed rock will often be planar or wedge failure (Figure 2.1). The GSI classification system assumes that the rock mass contains a sufficient number of "randomly" oriented discontinuities, allowing it to behave as an isotropic mass (Li et al., 2008). Combining a DFN with DEM better approximates the rock mass, whilst the orientations of these discontinuities are included, which massively influence its behaviour. However, DEM models come with additional computational time and gathering all the joint property data for the different joint sets in a DFN can be problematic.

Stochastically generated DFNs employ a statistical approach to modelling fractures as straight lines in 2D or planar discs/polygons in 3D. They are generated using probability density functions of geometric parameters, including orientation, size, and density. This statistical data can be collected by field surveying, such as borehole or outcrop mapping, manual selection of discontinuities in a 3D model, or geophysical methods, (semi-)automatic selection of discontinuity sets using a dedicated program. Fractures are generated in a model domain, with each property obeying specific statistical distributions (Lei et al., 2017). This stochastic approach allows for the creation of fracture network models that aim to approach the inherent complexity and variability of natural fracture systems while approaching hard conditioning data used to simulate the fracture network. However, because different fracture networks can attain the same statistical distribution, the strength of a rock mass can differ depending on the generated network. Therefore, multiple analyses have to be performed to understand the possible strength range of, in this case, a pillar. This is done by varying the model seed, a number used as an initial value for a random number generator. A unique seed will produce a unique DFN as the fractures are randomly generated whilst obeying the geometric parameters. Running models with different model seeds allows us to generate different DFNs and perform a stochastic analysis.

Within the DEM, blocks formed between fractures and bedding planes can be modeled as rigid bodies, deformable bodies, or using a BBM. This research utilises the BBM approach. In 3DEC, a BBM simulates the intact rock using bonded polyhedral elements, such as tetrahedrons or Voronoi elements. These elements are modelled elastoplastic with infinite yield strength with failure of the intact rock occurring at the contact between these elements. A BBM with tetrahedrons or Voronoi elements stands out from particle-based methods like PFC3D, which model the elements as spheres due to its capability to represent a condition of zero initial porosity ("Bonded Block Model in 3DEC," 2024). This allows the interlocking of irregular block shapes, which provides resistance to block rotation after contact breakage. This makes it particularly suitable for modelling the high uniaxial compressive strength (UCS) to tensile strength ratios and friction angles commonly found in hard rock. The BBM also has key advantages over traditional continuum approaches, including the ability to simulate spalling, support unidirectional bulking after breakage, and allow the initiation and propagation of cracks. These capabilities make the BBM a highly effective tool for modelling and analysing the complex behaviour of hard rock in mining applications. An example of this is the research from Suner and Tulu (2022), which used the two-dimensional Universal Distinct Element Code (UDEC) to look at the effect of different width-to-height ratios of pillars. They integrated a BBM with Voronoi elements and DFN model.

Previous research that uses numerical models to determine the stability of underground excavations often focuses on existing structures. (Tzalamarias et al., 2019) modelled an entire underground R&P coal mine in Greece whilst (Monsalve, 2019) focuses only on roof stability of a single tunnel in a limestone mine in the US. Modelling existing excavations enables the validation of the models by comparing the simulated rock mass behaviour with those observed in real life. Since this approach to model validation is not possible as this research is a preliminary mine design and no underground excavation exists, an alternative method for model validation is used. This study models a different scenario to test the model's effectiveness in simulating structurally controlled failure. Specifically, Phillipson (2012) examined a significant pillar collapse in an R&P mine with rock mass properties similar to those of the MLD quarry. This collapse suggests that the pillars should have a factor of safety (FoS) around 1. The model will be validated if it demonstrates a FoS close to 1. To validate the stress-controlled failure, a UCS test will be simulated, and the model will be calibrated to ensure the intact rock strength is similar to the one measured in the lab. The MLD quarry has, contrary to the rock mass in Phillipson (2012), bedding that is nearly sub-horizontal, and two joint sets that are sub-vertical, which makes failure along the discontinuities less likely. Still, the variation in fracture orientation within each set, combined with the 3D effect of the different discontinuities' orientations relative to one another and the pillar edges, justifies using a DFN to capture the full complexity of the rock mass behaviour.

3 Marches les Dames: Geological and Geotechnical modelling

The MLD quarry is located 10 kilometres East of Namur (Belgium) on the northern bank of the river Meuse. The rock in the quarry consists of dolostone of six different geological layers and includes gently dipping bedding planes and two sub-vertical joint sets. The area also features zones of significant weathering. All these features contribute to a heterogeneous rock mass, which necessitates the quarry's subdivisions into geotechnical units, each with relatively uniform rock mass properties. This chapter will provide an overview of the geology, including the depositional environment and the tectonic evolution, followed by an overview of the data from Jolly (2024).

3.1 Geology

3.1.1 Depositional environment

During the Lower Carboniferous, the Namur-Dinant Basin (NDB), located south of the Brabant Massif, accumulated carbonates (Bless et al., 1983). These deposits connected geographically with the south-western United Kingdom and potentially the German Kulm Basin during the Tournaisian and early Viséan periods (Poty, 2016). The basin's sedimentary record is characterised by shallow marine limestones, with notable occurrences of dolomitisation in Tournaisian deposits (Nielsen et al., 1994). Poty (2016) divided the NDB into seven distinct palaeogeographic areas, emphasising their unique tectonic-sedimentary evolutions. The formations in the MLD quarry consist of dolostone and are part of the Namur Sedimentational Area (NSA) (Figure 3.1). They were deposited during the Dinantian (359 to 326 million years)(Poty, 2016). The three main formations within the quarry are the Terwagne, Longpre, and part of the Engihoul formations. These dolomitised deposits are assigned to the Namur Group and are illustrated in Figure 3.2. Contrary to the Terwagne formation, the Longpre and Engihoul formations exhibit discontinuous bedding planes attributed to replacement dolomitisation (van der Voet et al., 2022), which happened during the early Visean.

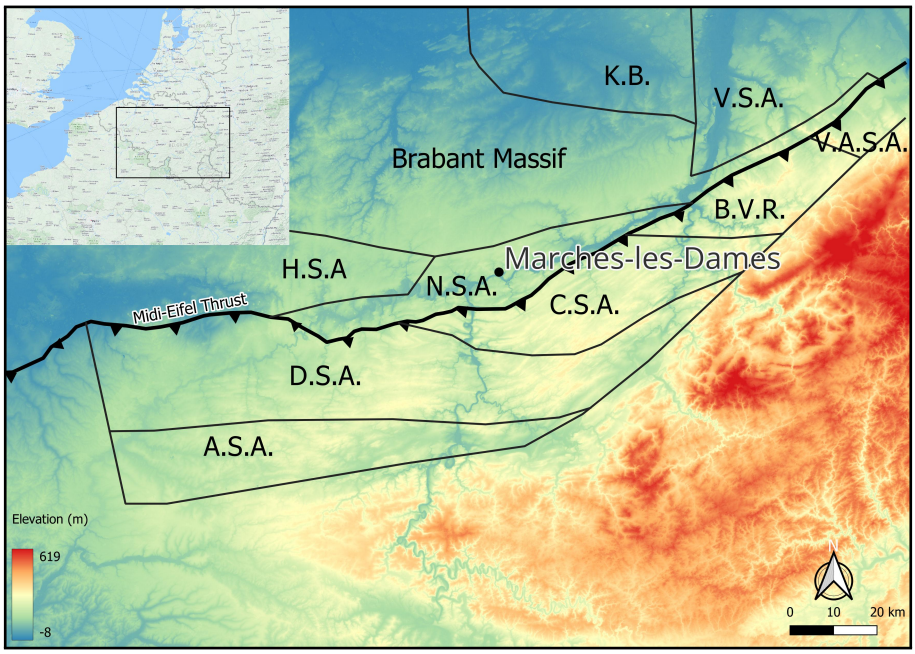

Figure 3.1: Dinantian sedimentation areas in the Namur-Dinant Basin (redrawn from Poty (2016)). ASA: South Avesnois sedimentation area, BVR: Booze – Le-Val-Dieu ridge, CSA: Condroz sedimentation area, DSA: Dinant sedimentation area, HSA: Hainaut sedimentation area, KB: Campine Basin, NSA: Namur sedimentation area, VASA: Vesdre – Aachen sedimentation area, VSA: Visé – Maastricht sedimentation area.

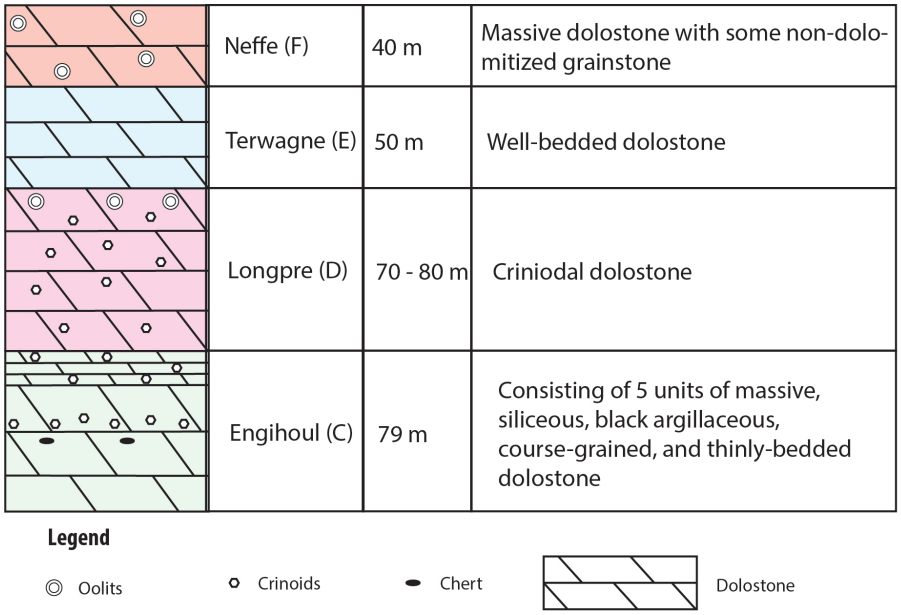

Figure 3.2: Stratigraphic column of the Marche-Les-Dames quarry (Poty, 2016)

3.1.2 Tectonic evolution

During the Variscan orogeny, a large northwestwards thrust fault referred to as the Midi-Eifel thrust developed due to the thrusting of the Ardennes Allochton (area South of the fault) over the Brabant parautochthon (area North of the fault) (van der Voet et al., 2022). The rigidity of the Brabant parautochthon prevented any large deformations within the MLD area (Robert, 1989) contrary to the area South of the Midi-Eifel thrust, which is more folded and faulted. The two sub-vertical joint sets in the MLD quarry are oriented 300/80 (J1) and 019/80 (J2) (Figure 3.3). Their origin is unclear, but they show similarities with the two joint sets in the Soignies quarry just over 50 km northwest of the MLD quarry. These two sets in the Soignies quarry are related to a regionally extensional period during the Cretaceous-Tertiary (Vandycke, 1997). Therefore, it is plausible that the J1 and J2 joint sets have the same origin, but this can not be confirmed. The only certainty is that they formed after the dolomitisation (van der Voet et al., 2022).

3.2 Geotechnical units

The data to generate the DFN is from Jolly (2024). During the research, the goal was to make a quantitative joint characterization of the study area and generate a quarry-wide DFN. The first part involves data collection from rock core descriptions, virtual outcrop mapping and field investigation. When a field or 3D survey is performed on an irregular rock mass with discontinuities visible on slopes with different orientations, the resulting data will give a good representation of the fracture network (Terzaghi, 1965). However, when a linear sampling technique such as a scanline or borehole is used, the acquired data can be misleading. Discontinuities parallel to the sampling orientation will be excluded from the data. Weighting factors to reduce this bias of the sampling line will not always resolve this problem, while orientations that are not measured are not recovered by these factors (Park & West, 2002). Therefore, the three different methods applied by Jolly (2024) for a quantitative joint characterization should make for a robust data set.

Jolly (2024) also documented the appearance of several geological features in the quarry which could affect the stability of an underground excavation. Small karstic voids are present in the Longpre and Engihoul formations, which can have diameters ranging from 0.5 m to 2 m. These voids are often found with other geological structures, such as fracture corridors and faults. A fracture corridor is a zone with

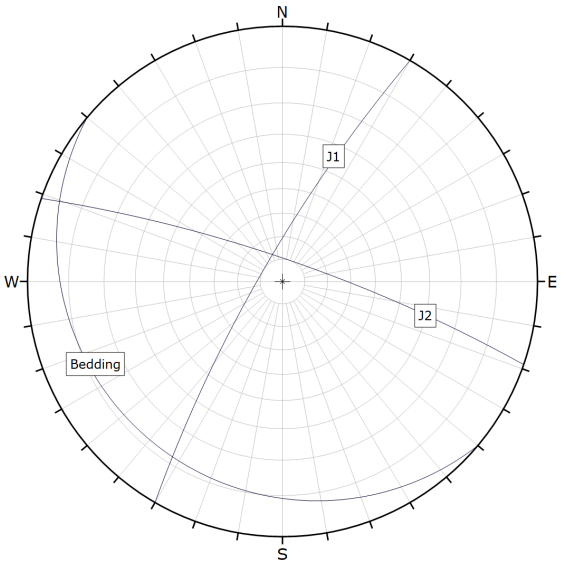

Figure 3.3: Equal angle and lower hemisphere projection of the bedding plane and two joint sets (J1 & J2) in the MLD quarry. This is only the average orientation with data from Jolly (2024).

a high intensity of fractures compared to the surrounding rock mass. The rock mass in this zone is often altered as it is a zone of higher permeability, allowing more fluid to run through the rock. This zone, therefore, has more joints with clay and dolomitic sand infill. These dissolution joints commonly have a width of around 10 cm but can be up to 2 m. Another karstic phenomenon observed in MLD is the pinnacle zone. This zone is a vertical rock formation often found in karstic regions. The material above this zone consists of fine-grained sediments to large pebbles. There are no major faults within the quarry.

The data to generate the DFN is for both joint sets (J1 & J2) divided into structural and background joints. The division accounts for the joint's impact on the pillar's structural integrity. A structural joint is a joint that extends at least 6 m on the surface, with background joints being smaller than 6 m. When joints have an aperture larger than 10 cm, they are considered a weakness zone and will not be included in the DFN and, therefore also not in the 3DEC model.

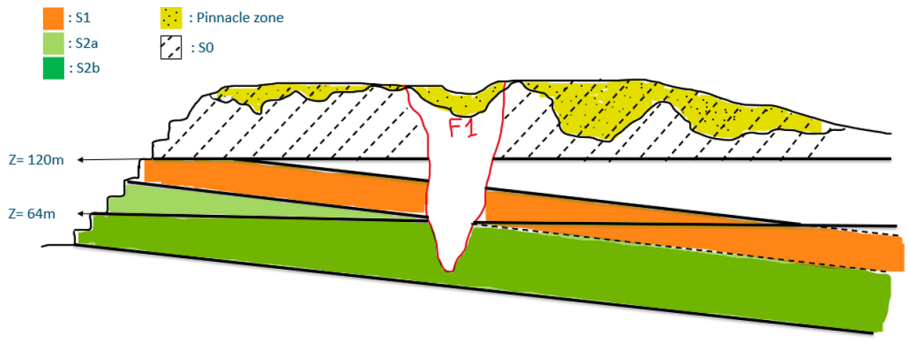

Figure 3.4: A schematic cross-section displaying the different geotechnical units within the quarry (Jolly, 2024)

Jolly (2024) divided the MLD quarry into four geotechnical units based on similar geotechnical properties such as joint orientation, conditions, or intensity. Each of these units is part of a sub-vertical fault domain (F) or part of a stratigraphic domain (S). There are two units in the fault domain (F1 & F2), but because they have similar rock mass properties, they are considered the same unit. The F domain is highly karstified and runs vertically through the geological layers and thins out towards the bottom of the quarry (Figure 3.4). The rock in this domain is highly weathered, with karst voids being filled with silt clay, and the fracture intensity is higher than the other domains. The S domain is divided into S0, S1, S2a and S2b. The S0 unit consists of superficial karst and sand pockets and is economically not interesting for the operation. The S1 unit sits below S0 and consists of the Terwagne formation, as the bedding plane is thinner than the Longpre and Engihoul formations. The exact thicknesses will be discussed in Chapter 5. The S2 unit, consisting of the Longpre and Engihoul formations, is divided into two sub units due to differences in joint condition. The divide is located at the natural water table, with the S2a having worse joint conditions than S2b.

4 Failure Mechanisms in Room and Pillar Mines

Numerically modelling a heterogeneous rock mass necessitates simplifying the real world. This requires a good understanding of the relation between all possible failure mechanisms and rock mass properties. This understanding also includes how changes in these properties could influence the stability of the underground excavation. This knowledge can then be applied to simplify the rock mass, reducing computation time but keeping the necessary parameters to correctly model the rock mass behaviour.

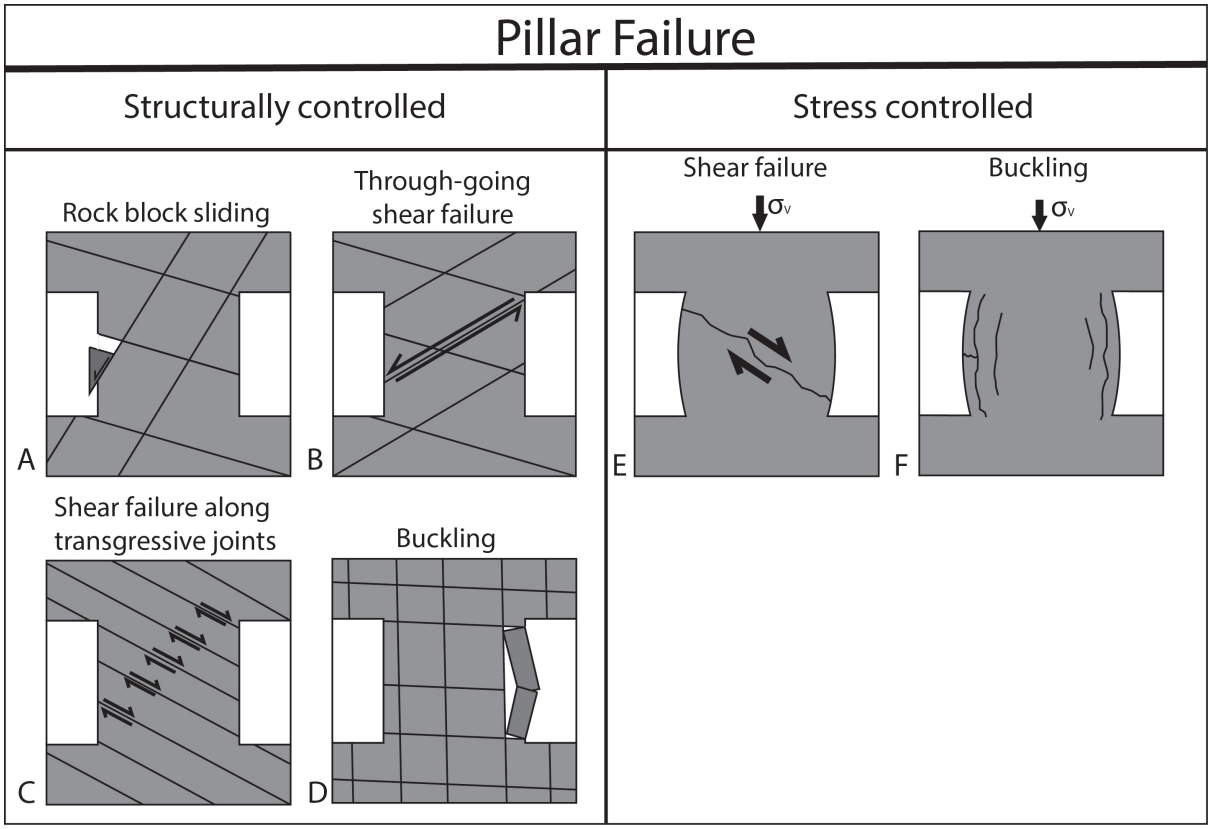

Figure 4.1: Possible failure modes within a pillar (Lunder, 1994)

The first step is to divide the failure mechanisms into two types of failure: stress and structurally controlled failure. Both failures can affect the pillars and roof (Lunder, 1994, NIOSH, 2011). For pillar failures (Figure 4.1), structurally controlled failures include (A) rock block sliding, where individual blocks move; (B) through-going shear failure, where a single discontinuity cross-cuts the pillar, causing failure; (C) shear failure along transgressive joints, which occurs when multiple discontinuities lead to failure; and (D) buckling of pillar segments due to sub-vertical joints and high vertical stress. The stress-controlled failures in pillars include (E) shear failure and (F) buckling due to excessive loads. For roof failures (Figure 4.3), structurally controlled mechanisms include (A) rock block sliding or falling, which happens when discontinuities intersect; (B) failure of bedding-related roof beams due to sub-horizontal discontinuities, where the beam cannot support its own weight; and (C) caving of weak overlying strata, where weaker rock or rock mass properties can cause a collapse. Stress-controlled roof failures involve (D) roof beam buckling due to excessive horizontal stress.

4.1 Pillar

4.1.1 Structurally controlled failure

The stability of the four structurally controlled failure modes illustrated in Figure 4.1 is heavily influenced by the dip angle and density of the discontinuities. When looking at through-going shear failure (B) and shear failure along transgressive joints (C), sub-horizontal and sub-vertical discontinuities will not cause major instability risks while they will not allow any planes to slide under vertical stress. All intermediate dip angles could cause one of these two failure modes to occur. The sub-vertical discontinuities can cause minor issues for rock block sliding (A) due to the sliding of relatively small blocks at the side of the pillar. Contrary to the first three failure modes, buckling (D) is only a consequence of sub-vertical discontinuities. The likelihood of experiencing all four failure modes increases when the discontinuity density is higher.

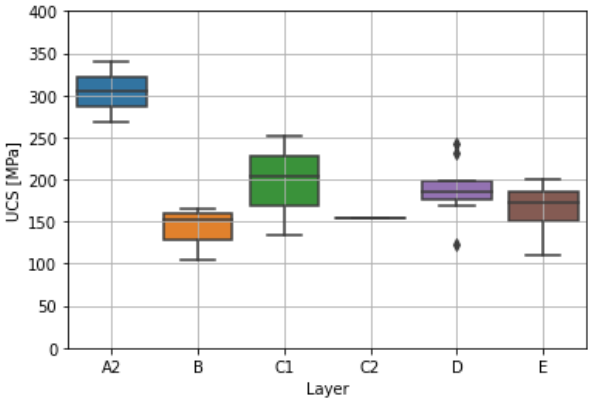

Figure 4.2: UCS strength of the unweathered samples (Jolly & Oostman, 2023)

All of these correlations between the failure modes and discontinuities are incorporated in the pillar strength equation of NIOSH (2011). In their equation (Equation 5.8), they do not consider discontinuities with dip angles below 30°, high dip angles have a lower influence, and an increase in discontinuity density also harms the pillar strength.

The three major discontinuities within the quarry are the sub-horizontal bedding and two sub-vertical joints (J1 & J2). J1 and J2 can be problematic for failure modes A and D. However, as discussed, rock block sliding due to sub-vertical joints will not greatly impact the pillar stability as the sliding blocks are relatively small.

4.1.2 Stress controlled failure

All stress-controlled failure modes, shear failure (E) and buckling (F), directly relate to the intact rock properties and the amount of stress.

The unweathered tested rock samples have an average Unconfined Compressive Strength (UCS) of 150 MPa or above (Figure 4.2) and are considered relatively strong based on the range of medium strength rocks in the research of NIOSH (2011) between 82 - 207 MPa. The overburden pressure is calculated using Equation 4.1 with the density (ρ) being 2834 kg/m^3 (derived from the laboratory tests) and the overburden depth (z) being 150 m, resulting in an overburden stress of 4.2 MPa. Rib spalling, which is characterised by fractures through the intact rock perpendicular to the pillar surface, can occur when the average pillar stress exceeds $11\% - 12\%$ of the UCS (NIOSH, 2011). Depending on the extraction ratio, this is a stress that can occur in the underground R&P in MLD. Important to note that this $11\% - 12\%$ of the UCS is the lower bound at which rib spalling can occur, which can also be caused by bad blasting practices that will not be considered in this research. The strength of the weathered rock is difficult to determine because of the heterogeneity of the F domain. In addition, few weathered cores have been cored because of their low strength, making retrieving them difficult. Only four weathered samples were tested. This low number of data and, therefore, the high uncertainty on the weathered intact rock strength should be taken into account when viewing the pillar and roof dimensions for the F domain.

$$\sigma_v = \rho \times g \times z \tag{4.1}$$

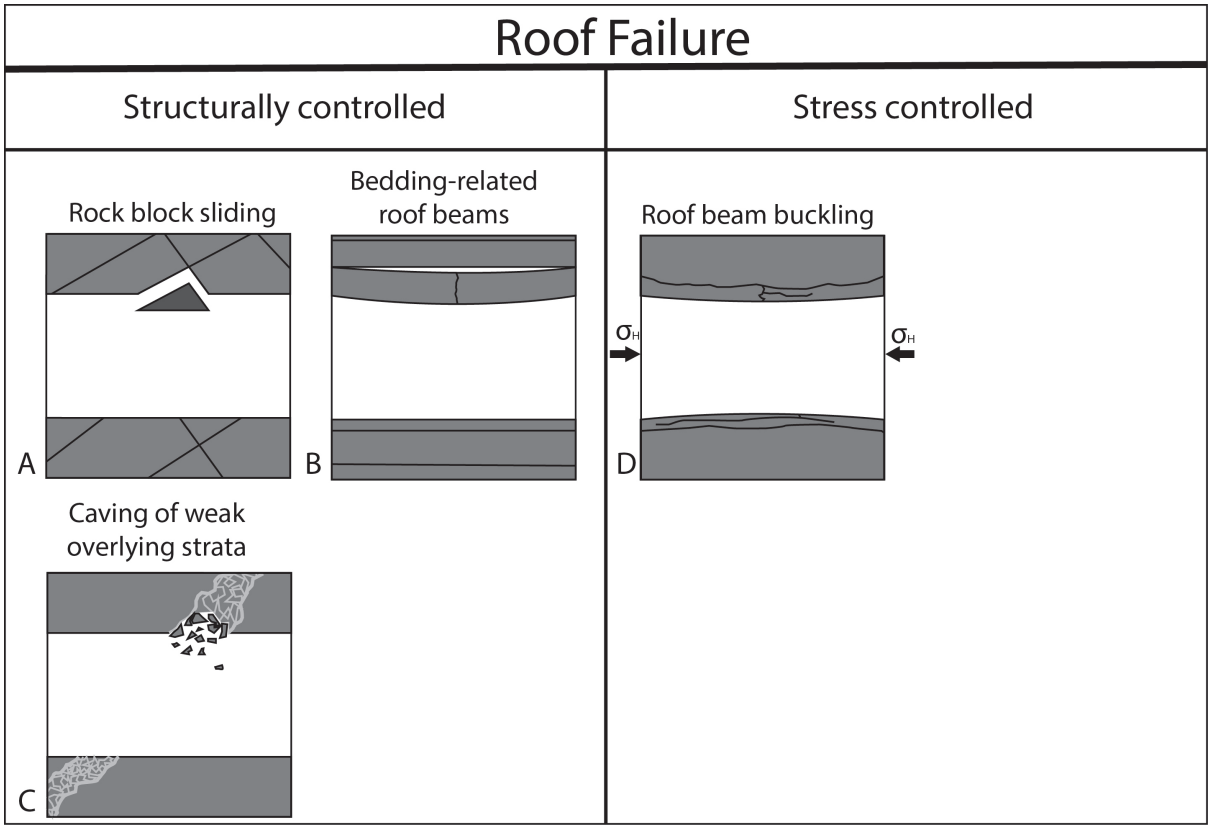

Figure 4.3: Possible failure modes within the roof (NIOSH, 2011)

4.2 Roof

4.2.1 Structurally controlled failure

Four distinct discontinuities are necessary to form a separate block for rock block sliding or falling to take place. Alternatively, this configuration can be achieved within an underground excavation having three discontinuities, with the fourth one represented by the excavated surface. Hoek (1977) presented a kinematic analysis using a stereo-projection that requires the input of the discontinuity orientation and dip angle as well as the friction angles of the discontinuities. However, the friction angle is only required when the block detaches by sliding along any of the adjacent blocks. Therefore, structurally controlled failure by rock block sliding (Figure 4.3 (A)) is dependent on the discontinuity orientations and possibly the friction angle. Bedding-related roof beam failure (Figure 4.3 (B)) is mainly related to the bedding thickness as well as the tensile strength of the intact rock. NIOSH (2011) advises the roof beam to be at least 1.2 meters thick. In their analysis, 82% of the locations that have a roof beam thickness of 1.2 meters or lower show stability issues. It is important to note that these issues can also be caused by sub-horizontal discontinuity sets. The final structurally controlled failure mode for the roof is the caving of weak overlying strata (C). Weak strata can relate to many features, such as weak geological layers, weathered rock, fracture corridors and bad blasting. All areas of the rock mass that are weaker than the surrounding rock mass can initiate this failure.

There are three distinct discontinuity sets present within the quarry, making failure mode A potentially a risk. The different geotechnical units vary in bed thicknesses due to differences in sedimentation, dolomitisation, and weathering. Information on the bedding spacing is available but has to be handled with care because of the dolomitisation. This process has caused the beds to become discontinuous, making them difficult to measure and identify, potentially obscuring internal planes of incipient weakness. Given that these bedding features could compromise roof stability, the data should be handled conservatively when used in the empirical method to determine the maximum roof span. Therefore, the thinner

spacing is chosen when a range on the bedding plane thickness is given for the distinct geotechnical unit.

Dissolution joints in the quarry can consist of dolomitic sand or clay and vary greatly in size (Jolly, 2024). When these joints are present in the roof, failure mode C is likely to occur, and support measures such as shotcrete or steel mesh have to be installed depending on the severity. However, the occurrence of these joints is extremely difficult to predict.

4.2.2 Stress controlled failure

Stress-controlled failure by roof beam buckling (D) is directly related to the intact rock properties. Weaker rock will be more subjected to buckling of the roof, which can already occur at depths of only 45 meters, as was observed in one case of the research of NIOSH (2011).

5 Methodology Empirical R&P Mine Design and 3DEC Pillar Modeling

The methodology chapter is structured into three main sections. The first section provides an overview of the tools used in this research. This includes the two empirical methods, the Q-System and the R&P design guidelines (NIOSH, 2011), as well as the distinct element method (DEM) software 3DEC with integrated DFN. The second section outlines the research design, detailing how the empirical methods are applied to determine the R&P dimensions, after which the pillar dimensions are modelled and tested to determine their strength.

5.1 Research Tools

5.1.1 Empirical equations

5.1.1.1 Q-System

The Q-System is a rock mass classification developed by the Norwegian Geotechnical Institute (NGI) (NGI, 2022). The system is used for the classification of the rock mass around an underground opening and for field mapping for hard, jointed rocks, including weakness zones. The Q-value is based on six parameters and has a value between 0.001 and 1000:

$$Q = \frac{RQD}{J_n} \times \frac{J_r}{J_a} \times \frac{J_w}{SRF} \tag{5.1}$$

The six parameters are:

1. RQD = Rock Quality Designation
2. J_n = Joint set number
3. J_r = Joint roughness number
4. J_a = Joint alteration number
5. J_w = Joint water reduction factor
6. SRF = Strength Reduction Factor

Each of the three fractions of Equation 5.1 describes the three main factors that influence the stability of an underground opening, which are:

the degree of jointing:

$$\frac{RQD}{J_n} \tag{5.2}$$

the joint friction:

$$\frac{J_r}{J_a} \tag{5.3}$$

and the active stress:

$$\frac{J_w}{SRF} \tag{5.4}$$

It is important to note that when applying the Q-System to determine the roof span for an underground R&P, the joint set number (J_n) has to be applied by 3 to account for tunnel intersections. This is because of the extra degrees of freedom that the blocks can move at an intersection. In addition to this, the span has to be divided by the Excavation Support Ratio (ESR) to account for the safety requirements for the excavation:

$$\frac{\text{Span or height in m}}{ESR} = \text{Equivalent dimension} \tag{5.5}$$

The type of excavation for R&P operations falls under type C: 'Permanent mine openings, water tunnels for hydropower (exclude high-pressure penstocks), water supply tunnels, pilot tunnels, drifts and headings for large openings'. The equivalent ESR for this type is 1.6 and is therefore used in Equation 5.5. As NGI (2022) mentions, it is advised to divide the excavation area into several sections to limit the range of Q-value in each section. This is also done in this study as the mine is divided into geotechnical units having similar geotechnical properties.

5.1.1.2 Pillar and Roof Span Design Guidelines for Underground Stone Mines

The empirical research included 34 different stone mines in the Eastern and Midwestern United States. At each location, data on excavation dimensions, rock jointing characteristics, rock mass classification, and excavation stability conditions were recorded. Several of these mines include limestone with rock strengths well within the range of the MLD quarry (44-301 MPa). They give guidelines for the roof span and the location of the roofline relative to the bedding planes or lithology changes and use the pillar strength Equation 5.8, to determine the pillar strength. It consists of a base equation that considers factors like confinement, pillar shape, and volume:

$$S = k \times \frac{w^{0.30}}{h^{0.59}} \tag{5.6}$$

where w is the width, and h is the height of the pillar. The strength parameter k is expressed in terms of UCS:

$$k = 0.65 \times UCS \tag{5.7}$$

The final formula that accounts for the inclination and spacing of large angular discontinuities is as follows:

$$S = 0.65 \times UCS \times LDF \times \frac{w^{0.30}}{h^{0.59}} \tag{5.8}$$

where the Large Discontinuity Factor (LDF) is added to the equation. The LDF is determined by combining a Discontinuity Dip Factor (DDF) (Table 5.1) with the frequency of the discontinuities, the Frequency Factor (FF) (table 5.2):

$$LDF = 1 - DDF \times FF \tag{5.9}$$

	Pillar width-to-height ratio								
Dip (°)	≤ 0.5	**0.6**	**0.7**	**0.8**	**0.9**	**1.0**	**1.1**	**1.2**	**>1.2**
30	0.15	0.15	0.15	0.15	0.16	0.16	0.16	0.16	0.16
40	0.23	0.26	0.27	0.27	0.25	0.24	0.23	0.23	0.22
50	0.61	0.65	0.61	0.53	0.44	0.37	0.33	0.30	0.28
60	0.94	0.86	0.72	0.56	0.43	0.34	0.29	0.26	0.24
70	0.83	0.68	0.52	0.39	0.30	0.24	0.21	0.20	0.18
80	0.53	0.41	0.31	0.25	0.20	0.18	0.17	0.16	0.16
90	0.31	0.25	0.21	0.18	0.17	0.16	0.16	0.15	0.15

Table 5.1: Discontinuity dip factor (DDF) (NIOSH, 2011)

LDP	0.0	0.1	0.2	0.3	0.5	1.0	2.0	3.0	≥ 3.0
FF	0.00	0.10	0.18	0.26	0.39	0.63	0.86	0.95	1.00

Table 5.2: Frequency Factors (FF) for Large Discontinuities per Pillar (LDP) (NIOSH, 2011)

The frequency factor of large discontinuities per pillar can be determined by dividing the pillar width by the average spacing of the large discontinuity. When there is more than one set, the density of both sets is combined, and the same calculation is performed. This factor does, therefore, not take into account the orientation of the two joint sets with respect to each other.

According to empirical research, the pillar should have a FoS not less than 1.8 and a width-to-height ratio not lower than 0.8. Thinner pillars are more susceptible to being cross-cut entirely by a discontinuity (failure mode B (Figure 4.1)), and the lack of confinement in the core makes them inherently weaker.

5.1.2 Discrete Element Method

A DEM model allows for the discretisation of the model into an assemblage of discrete blocks that can separate and rotate relative to each other. This method was first introduced by Cundall (1971) and extended by Cundal and Strack (1979) to incorporate the simulation of granular soils. The first DEMs only allowed the modelling of discrete elements as rigid bodies but extended into the discrete element method for deformable bodies (DEM-FD), also called the finite discrete element method (FDEM). This allows for the analysis of a rock mass, looking into the possibility of structural or stress-induced failure simultaneously.

3DEC uses a dynamic algorithm with an explicit time-stepping method to simulate the mechanical behaviour of the discontinuous system ("Introduction — 3DEC 7.0 documentation," 2014). The software tracks the motion and forces of each block, updating their positions and velocities based on Newton's second law of motion. Additionally, 3DEC incorporates contact detection algorithms to accurately model the contact forces and interactions at block interfaces, ensuring realistic simulation of rock mass behaviour. Natural dynamic systems contain some degree of damping of vibrational energy. If there is no damping, a system will oscillate indefinitely. In 3DEC, damping occurs partly due to energy loss from slippage along contacts between blocks, internal friction within the intact material, and resistance from air or fluids surrounding the structure. It is important to have sufficient damping in the model whilst the system should remain in quasi-static conditions (unbalanced force ratio remains low). 3DEC includes various damping modes, with each mode useful for various applications. The modes used in this research are discussed in 5.2.2.

5.1.3 Discrete Fracture Network

Representing fractures within a rock mass explicitly poses a considerable challenge. Direct observations of natural fractures are limited to lower-dimensional data like borehole logging and outcrop mapping and, therefore, require a stochastic approach (Lei et al., 2017). This approach requires probability density functions of geometric parameters to model the fractures, including orientation, size, and density (Jing & Stephansson, 2007). The orientation is modelled by the dip direction, dip angle, and Fisher orientation distribution to account for the spread in orientation for a single discontinuity set. The size is determined by the minimum length, maximum length, and power-law length distribution. The density is quantified by the number of fractures per unit length (P10 (m)), per unit area (P21 (m^2)), or unit volume (P32 (m^3)). P10 is often determined from one-dimensional measurements such as boreholes or scanlines as P10 is 1D data. A scanline involves laying out a straight line on an outcrop and then systematically measuring each intersection of a fracture from a single set on that line. P21 is measured from a surface, such as the wall of an open-pit quarry, while P32 is measured within a three-dimensional volume.

Fractures are modelled as discrete, planar elements with finite dimensions. In three-dimensional space, fractures are typically modelled as disks, although they can also be planar convex polygons. In two-dimensional modelling, fractures are represented as line segments, where vertex objects correspond to the endpoints of these segments (Itasca, 2024). Within 3DEC, a DFN consists of a single discontinuity set, but multiple DFNs can coexist in the same model. This separation into distinct DFNs enables the independent analysis of fractures with different characteristics. For instance, fractures can be categorised into sets based on their orientations or other defining attributes. An example of research that used 3DEC with DFN to approximate the behaviour of the rock mass is Soni et al. (2022). The research used laser scanning to produce a point cloud on which the discontinuities were mapped using the point cloud processing software I-Site Studio. Four discontinuity sets were modelled in the model, and a pillar with various karst voids was modelled to look at the effect of the voids on the pillar strength. An example where 3DEC was used to look at the roof stability is Monsalve (2019). The same method as Soni et al. (2022) was applied to gather the discontinuity data for the DFN. The blocks that failed from the roof in the model were compared with the failed blocks in the quarry. The 3DEC results showed good agreement with the field observation, displaying the strength of approximating the rock mass behaviour with a DFN.

5.2 Research Design

First, the maximum roof span is determined, followed by the pillar dimension. This order is crucial for determining the biggest possible pillar dimensions necessary to create the most stable excavation. Galvin (2016) compared two plan layouts for an underground R&P mine. One layout is a board and pillar with a pillar width of 12 m and a room width of 6 m (Figure 5.1 a). The second is a partial pillar extraction layout with a pillar width of 30 m and a room width of 6 m in one direction and 26 m in the other (Figure 5.1 b). The two layouts have the same extraction ratio and average pillar stress. However, the second layout resulted in more than doubling the pillar FoS. The two layouts are different, but the essence is the same: an increase in pillar dimension with similar pillar stress will result in a higher FoS. Therefore, the largest roof span has to be determined to create the largest pillar dimensions possible. This can also be derived from Equation 5.8. The DDF increases with an increase in pillar width-to-height ratio (Table 5.1), which will improve the LDF (Equation 5.9) and, therefore, also the pillar strength. This added strength is attributed to the increased confinement of weaknesses and discontinuities in the pillar.

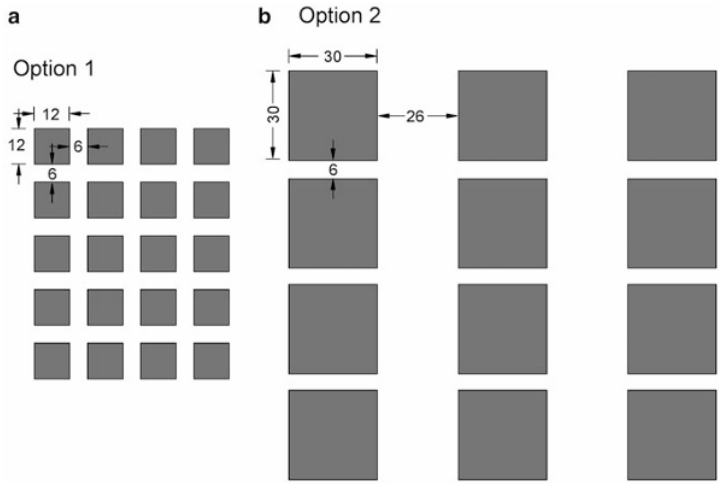

Figure 5.1: Displaying the difference between a board and pillar layout (a) and a partial pillar extraction layout (b) from Galvin (2016)

The roof dimensions will be determined using a combination of the Q-system and the R&P design guidelines from (NIOSH, 2011). The advantage of the Q-system is that it allows for investigating different roof spans for different support measures. However, the system's applicability is relatively broad, encompassing diverse rock masses in underground openings. In contrast, the R&P design guidelines are tailored explicitly for R&P hard rock mines. By combining these two approaches, we aim to achieve reliable results when applying the empirical methods. Subsequently, the numerical method is used to model a pillar with the dimensions determined using the empirical methods. The pillar is loaded until failure, and its strength is compared to the strength of the empirically determined pillar strength. Figure 5.2 is a simple workflow overview. The dimensions that are determined by applying the empirical method will consist of all four units: S1, S2a, S2b and F. The numerical method will only focus on the S1 and S2a units because the computational time is too high to model all four geotechnical units. It has been chosen to model the S1 and S2a units because data on the intact rock of the F unit is limited and because the S2a and S2b have more similar rock mass properties than the S1 and S2a units.

5.2.1 Empirical approach

5.2.1.1 Roof Span

The Q-system and the R&P guidelines are first used to determine the maximum roof span, only allowing rock bolting for support. The chart depicted in Figure 5.3 is used for this purpose. Two factors must be

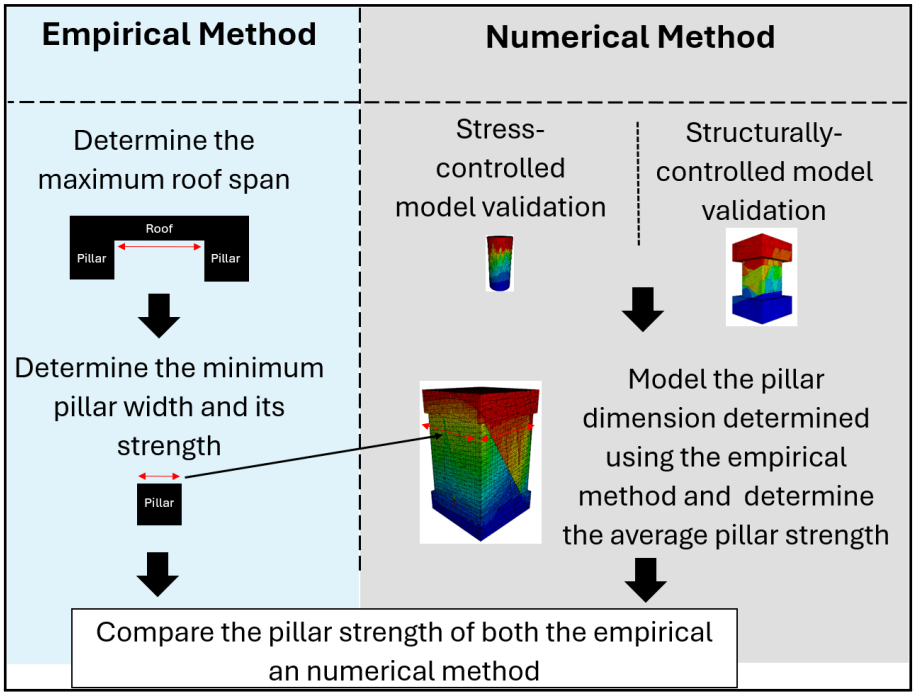

Figure 5.2: Research workflow

taken into account when using the Q-system for this application. First, the roof span, indicated on the left Y-axis in Figure 5.3, has to be divided by the ESR value of 1.6. Secondly, at intersections, which is the case in an R&P mine, the J_n has to be multiplied by three as recommended by NGI (2022). This reduces the Q-value and reduces the roof span. Because the roof span at an intersection is larger and its Q-value of the rock mass is reduced by a factor of three, the roof span is mainly determined by the span of the intersection. The span and support measures determined from Figure 5.3 will be compared with the guidelines from NIOSH (2011) and improved if necessary.

5.2.1.2 Pillar dimensions

Two equations are used for determining the pillar width: the pillar stress equation (Equation 5.10) and the pillar strength equation (Equation 5.8). The pillar stress equation is multiplied by the FoS to get the pillar strength (Equation 5.11). We can calculate the pillar width by setting both sides of the different pillar strength equations equal and applying the criteria — FoS > 1.8, width-to-height > 0.8. Appendix 11.3 provides details on the Python solver used for these calculations.

$$\sigma_v = \rho \times g \times z \times \frac{(w_o + w_p)^2}{w_p^2} \tag{5.10}$$

5.2.2 3DEC model

The following part explains the numerical aspect of the research design, which consists of model validation and testing of the pillar dimensions determined by the empirical method. The model validation is subdivided into validating the structurally controlled failure and the stress-controlled failure. For all three models (two types of model validation and one MLD pillar loading), the zoned blocks are modelled as elastoplastic with infinite yield strength and the joints are modelled with the Mohr-Coulomb failure criterion. Before loading, the model is cycled until reaching equilibrium under its own gravity. The damping mode in this stage is 'Global', which is the fastest way to dissipate vibrational energy in static conditions ("block mechanical command — 3DEC 7.0 documentation," 2019). Various damping modes within 3DEC relate to different model types, such as static or dynamic. After equilibrium has been reached, the damping mode is set to 'Combined', which is, according to Sinha et al. (2022), the best

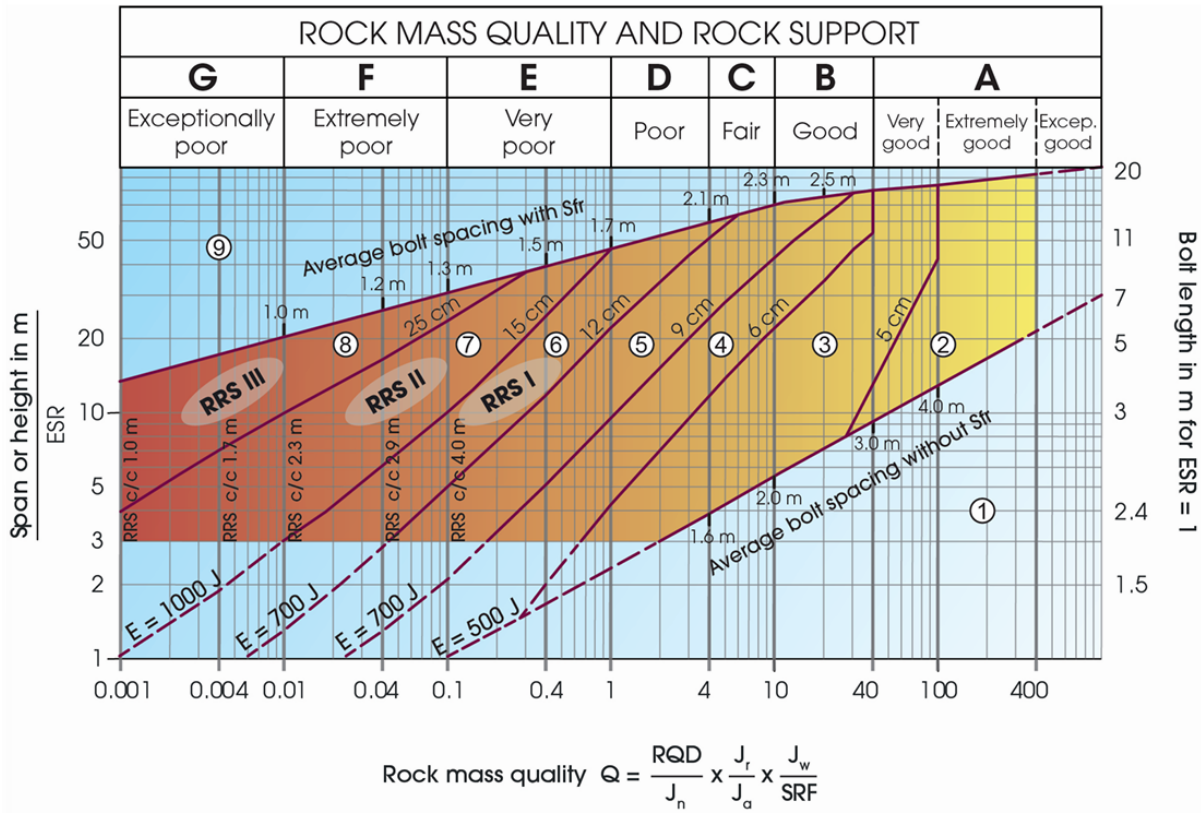

Figure 5.3: Rock Mass Quality and Rock Support (NGI, 2022)

damping mode for modelling dilation and bulking of pillars (dynamic model). This is because other damping modes, such as 'Local' damping, dampen the model too much, which hinders the separation of blocks, increasing the confinement and, therefore, the pillar strength. The loading in all three sections will be performed with a velocity of 0.5 m/s. Such a high velocity can be applied to the pillar because the software uses a dynamic, explicit time-stepping method ("Introduction — 3DEC 7.0 documentation," 2014). Additionally, the velocity is applied as gradually as possible, allowing the system to dissipate imbalances and maintain a mechanical ratio as low as possible.

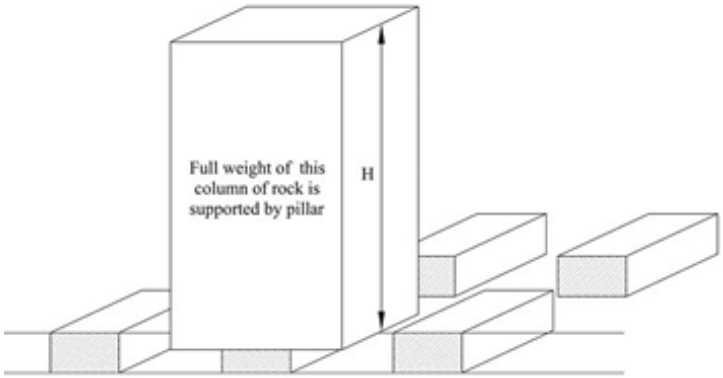

Figure 5.4: Tributary area load concept (image from Galvin (2016))

5.2.2.1 Model validation: Structurally controlled failure

The rock mass of Phillipson (2012) present similarities with the MLD rock mass, with a significant difference being the discontinuity dip angles. The bedding in the case study dips 20°, one discontinuity set 65°and another set 90°. The expected failure mode of this pillar is structurally controlled because of the joint set dipping 65°. Therefore, this part of the model validation will only focus on structurally controlled failure and not include a bounded block model (BBM), as this will add unnecessary complexity and computational time. Because the pillars in the study have failed, they are expected to have a FoS of around 1. The S-Pillar software, which uses the pillar strength equation from NIOSH (2011), calculated the FoS of the pillar to be 1.1. Therefore, the model will be considered validated if the 3DEC simulation of the pillar indicates a FoS close to 1 or 1.1.

The pillar strength will be determined by loading the pillar until failure. The pillar stress will be calculated using Equation 5.12, which assumes the concept of the tributary area load (TAL). TAL assumes that the pillar is carrying the entire column of overburden directly over its area of influence (Figure 5.4). This entire column is the pillar load in equation 5.12. The assumption of TAL results in an overestimated pillar stress, as it neglects the stiffness of the overburden. According to Galvin (2016), the real load will be around 95% of the TAL load for a pillar that has at least three pillars on either side up to the unexcavated area. Consequently, the average pillar stress in Equation 5.12 is multiplied by 0.95 to account for this, as is the case in this research.

$$FoS = \frac{\text{Pillar Strength}}{\text{Pillar Stress}} \tag{5.11}$$

$$\text{Pillar Stress} = 0.95 \times \frac{\text{Pillar Load}}{\text{Pillar Area}} \tag{5.12}$$

5.2.2.2 Model validation: Stress-controlled failure

The block size of a BBM should be small enough to accurately represent the failure path in the intact rock, but it is limited by computer memory and computational time. The minimal particle-to-specimen ratio should be 1/10 for laboratory UCS tests, according to ISRM (2007). This means that the diameter of the sample should be at least ten times bigger than the largest grain. This same ratio is applied in the BBM model, where the smallest blocks are at least ten times smaller than the pillar width, which is a similar approach used by Suner and Tulu (2022). The BBM in 3DEC simulates a rock mass using bonded polyhedral elements, such as tetrahedrons. These bonded polyhedral blocks can fracture along their subcontacts, with contact properties matching those of the intact rock. To meet the 1/10 ratio, the edge length of these tetrahedrons is set to 0.6 meters for the MLD case. Therefore, the UCS test that is simulated models a cylinder with a diameter of 6 m and a height of 14 m. This width-to-height ratio is the same for the UCS performed in the laboratory. The bottom of the sample will be fixed, the sides will have no boundary conditions, and the top will be loaded as described in 5.2.2.

When the UCS in the 3DEC model is not the same as the one in the laboratory, the cohesion of the tetrahedral contacts is adjusted accordingly, similar to the calibration of the UCS in Bahrani and Valley (2020). When the UCS is lower, the cohesion is increased. When the UCS is higher, the cohesion is decreased.

5.2.2.3 Pillar Dimensions

The pillar will be modelled using a DFN and a BBM model with the tetrahedral blocks having the same edges of 0.6 m to ensure the particle-to-specimen ratio of 1/10 as discussed in 5.2.2.2. The pillar will be modelled with a top and bottom cap of a quarter of the pillar height (Figure 5.5). To get to this geometry, an assemblage of blocks is cut to create the final pillar shape (Figure 5.6). This cutting process is important because tetrahedral zoning often causes aligned zones along the edges, resulting in unrealistically high strengths due to the structured arrangement of blocks along these edges. The difference in the aligned zones before and after cutting is clearly visible in Figure 5.6a & 5.6b. The bottom of the pillar is fixed, the sides of the caps have roller boundaries only allowing vertical movement, and the side of the pillar has no boundary conditions. Again the pillar will be loaded as described in

5.2.2. Because of the high computational time, the domains modelled using the DEM model will be restricted to the S1 and S2a domains with their mean intact rock properties.

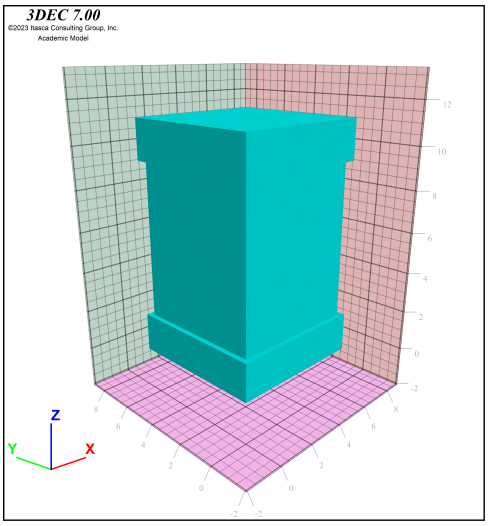

Figure 5.5: Pillar geometry for examining pillar strength

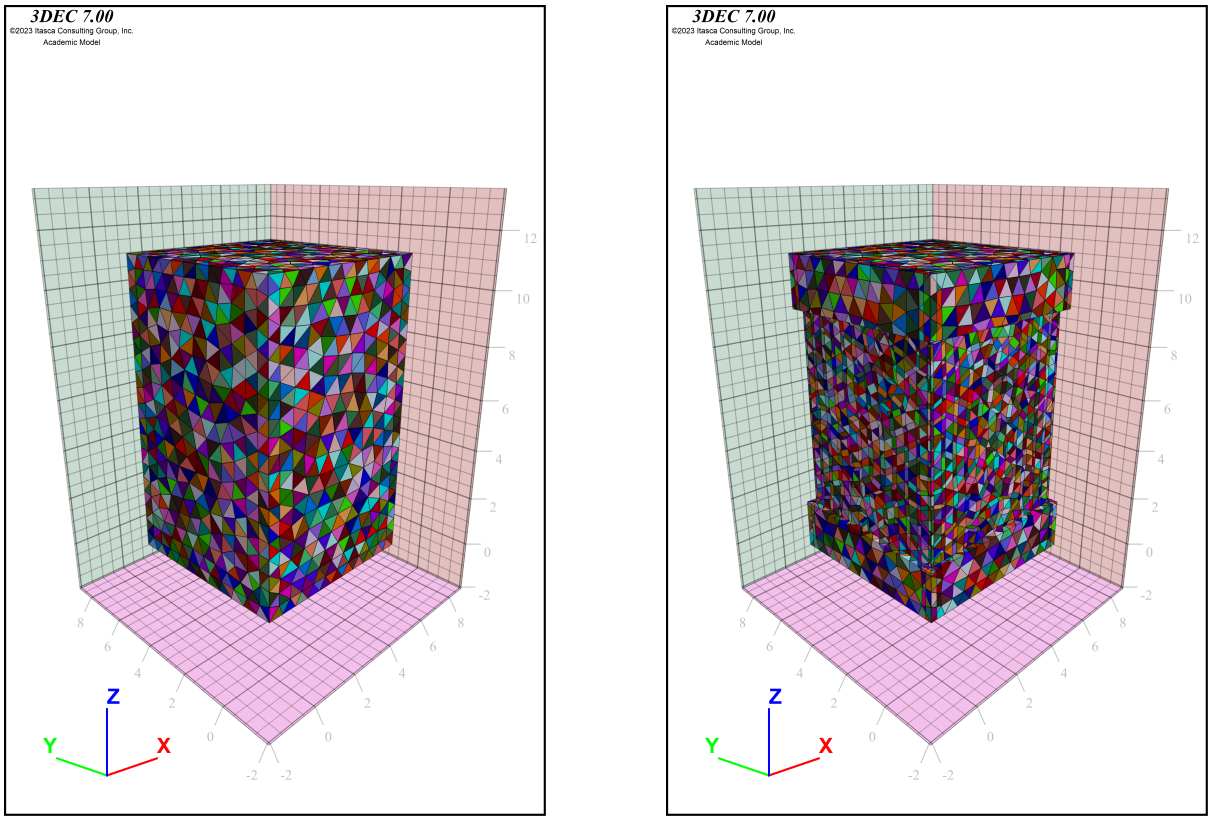

(a) (b)

Figure 5.6: 5.6a is the initial geometry that is cut to form the pillar geometry with top and bottom caps depicted in 5.6b. This step is crucial to prevent tetrahedral alignment at the sides, which is evident in 5.6a where similarly shaped triangles are visible. In contrast, the edges of the pillar in 5.6b differ in shape, preventing any large strengths due to the "crystalline" arrangement of blocks along these edges..

5.3 Parameters for MLD

This section will overview all parameters inserted into the numerical model. It will only focus on parameters that describe the properties of the intact rock and rock mass and their in situ stress, not the model dimensions, boundaries, and constitutive models.

Material properties	Density Young's Modulus Poissons ratio Tensile strength Cohesion Friction angle
Bedding	Dip direction Dip angle
DFN (J1 & J2)	Dip direction Dip angle κ (Fisher orientation distribution) α (power-law length distribution) Minimum length Maximum length P10/P21/P32
Contact properties	Normal stiffness Shear stiffness Friction angle Cohesion Tension
In-situ stress	Horizontal Vertical (overburden pressure)

Table 5.3: Material, bedding, DFN, contact properties, and in-situ stress parameters

5.3.1 Material properties

All the material properties are determined from lab tests and are displayed in Table 5.4. The intact rock properties assigned to unit F are the average of the weathered samples from the laboratory tests. This is probably an overestimation, as the cores that were too highly weathered were not retrieved or could not be made into a UCS sample. For the other three units, the average of the unweathered samples is used. The friction angle of the intact rock is calculated by using Equation 5.13 from Esterhuizen et al. (2013):

$$\phi = 0.090 \times UCS + 33 \tag{5.13}$$

This equation is suitable for limestone within the range of 40 - 200 MPa (UCS) and is based on a combination of triaxial testing from the Office of Mine Safety and Health Research and data available in the literature.

Table 5.4: Intact Rock Properties

Property	Unit	S1	S2a	S2b	F
UCS	MPa	182	182	182	69
Density	kg/m^3	2834	2834	2834	2834
Young's Modulus $E50_t$	GPa	67.6	67.6	67.6	40.1
Poisson's Ratio	-	0.22	0.22	0.22	0.31
Friction Angle	°	49	49	49	39
Cohesion	MPa	34	34	34	34
Tensile Strength	MPa	11	11	11	3.9

5.3.2 DFN

The input data on the bedding and the DFN is from Jolly (2024) and is displayed in Table 5.5. The data on the background joints is also presented but is not used in the numerical model.

5.3.3 Contact properties

The friction angle, normal stiffness (K_n), and shear stiffness (K_s) of the discontinuities are not measured and therefore need to be approximated. The friction angle can be calculated using the formula from Barton et al. (1974):

$$\text{friction angle} = tan^{-1}(J_r/J_a) \tag{5.14}$$

Both the joint roughness (J_r) and joint alteration (J_a) numbers are known for the J1 and J2 joints Jolly (2024). The calculated friction angle is displayed in Table 5.6. There is no data available to calculate the friction angle of the bedding planes. Because data on joint properties from field tests is extremely limited, the friction angle of 30° is chosen from Phillipson (2012). Because of the low dip angle of the bedding plane, it is not expected to cause failure, and its uncertainty will, therefore, not have a significant impact on the pillar strength.

The stiffness properties are derived from Bandis et al. (1983), which investigated the deformation characteristics of rock joints under normal and shear loading conditions. Tests were conducted on a diverse range of fresh and weathered joints from five different rock types. For the geotechnical units of the S domain, average values from slightly weathered limestone were used, and values from weathered limestone for the F domain. The limestone samples originated from the Lower Carboniferous formations in North Yorkshire.

5.3.4 In situ stress

There are no in situ stress measurements within the quarry. Therefore, measurements from the High-Activity Disposal Experimental Site (HADES) underground research laboratory are used as input parameters which is located 80 km north of the MLD quarry. The ratio of horizontal stress to vertical stress, represented by K, is 0.9 (NIRAS, 2001). This value is measured in the Boom Clay at a depth of 223 meters. The distance to the MLD quarry is just over 80 kilometres.

Table 5.5: DFN Input Parameters

Property	Unit	S1	S2a	S2b	F
Bedding					
Dip	°	11	11	11	11
Dip direction	°	220	220	220	220
Spacing	m	0.2–0.35	0.7–2.5–4	0.7–2.5–5	0.2–2.5–4
J1					
Dip	°	80	80	80	80
Dip direction	°	300	300	300	300
K-Fisher		45	45	45	45
Lmin	m	9	9	9	9
Lmax	m	30	30	30	30
Power law distribution length		1.25	1.2	1.2	1.2
P31		0.123	0.24	0.24	0.38
J2					
Dip	°	19	19	19	19
Dip direction	°	80	80	80	80
K-Fisher		35	35	35	35
Lmin	m	9	9	9	9
Lmax	m	30	30	30	30
Power law distribution length		1.25	1.4	1.4	1.3
P31		0.3	0.23	0.23	0.37
J1 (background)					
Dip	°	80	80	80	80
Dip direction	°	300	300	300	300
K-Fisher		45	45	45	45
Lmin	m	1	1	1	1
Lmax	m	10	10	10	10
Power law distribution length		1.6	1.6	1.6	1.425
P31		0.19	0.37	0.37	0.58
J2 (background)					
Dip	°	19	19	19	19
Dip direction	°	80	80	80	80
K-Fisher		35	35	35	35
Lmin	m	1	1	1	1
Lmax	m	10	10	10	10
Power law distribution length		1.6	1.4	1.4	1.425
P31		0.16	0.42	0.42	1.1

Table 5.6: Friction Angles of Discontinuities

Property	Unit	S1	S2a	S2b	F
Bedding					
Friction angle	°	30	30	30	30
J1					
Friction angle	°	37	37	37	37
J2					
Friction angle	°	33	33	33	33
J1 (background)					
Friction angle	°	42	42	42	42
J2 (background)					
Friction angle	°	42	42	42	42

Table 5.7: Stiffness Properties

Property	**Unit**	**S1**	**S2a**	**S2b**	**F**
Bedding					
Shear stiffness	GPa	29.3	29.3	29.3	5.8
Normal stiffness	GPa	18.8	18.8	18.8	8.5
J1					
Shear stiffness	GPa	29.3	29.3	29.3	5.8
Normal stiffness	GPa	18.8	18.8	18.8	8.5
J2					
Shear stiffness	GPa	29.3	29.3	29.3	5.8
Normal stiffness	GPa	18.8	18.8	18.8	8.5
J1 (background)					
Shear stiffness	GPa	29.3	29.3	29.3	5.8
Normal stiffness	GPa	18.8	18.8	18.8	8.5
J2 (background)					
Shear stiffness	GPa	29.3	29.3	29.3	5.8
Normal stiffness	GPa	18.8	18.8	18.8	8.5

6 Validation of 3DEC Numerical Model for Pillar Loading

This chapter focuses on the process of model validation to ensure the accuracy and reliability of the numerical simulations. The first section addresses the validation of structurally controlled failure by modelling a pillar from another quarry, which is known to have failed structurally. By comparing the model outputs to expected ranges of pillar strength, we assess the model's accuracy and its ability to predict structurally controlled failure. The second section focuses on stress-controlled failure mechanisms by simulating UCS tests using a bounded block model (BBM). The simulated peak stress is compared with laboratory results, and if they differ, the model is calibrated accordingly. Through these validation exercises, the chapter establishes the correct working of the numerical models.

6.1 Validating Structurally Controlled Failure

6.1.1 Model Input

The input parameters for the 3DEC model are displayed in Table 6.1. The input parameters for the DFN were an approximation based on the description of the joints and images from the pillars. Phillipson (2012) describes that the pillars in the failed area can have joints cross-cutting the pillar. Therefore, the fracture length was chosen to vary from 4 m to 20 m, allowing the possibility of fractures to be created that cross-cut the pillar. The scale of the image displaying a pillar face in Figure 6.1 is roughly estimated based on the pillar sizes. The generated fracture network was compared until the fractures roughly corresponded with the image. This is a big approximation; therefore, the DFN data has a large error. The intact rock strength properties are based on core samples from a marble mine in the same formation approximately 8 km away. As outlined in 5.2.2.1, the model is considered to be validated when the pillar strength has a FoS of 1.0 or 1.1. This coincides with a pillar strength of around 15.0 - 16.5 MPa (taking into account the TAL).

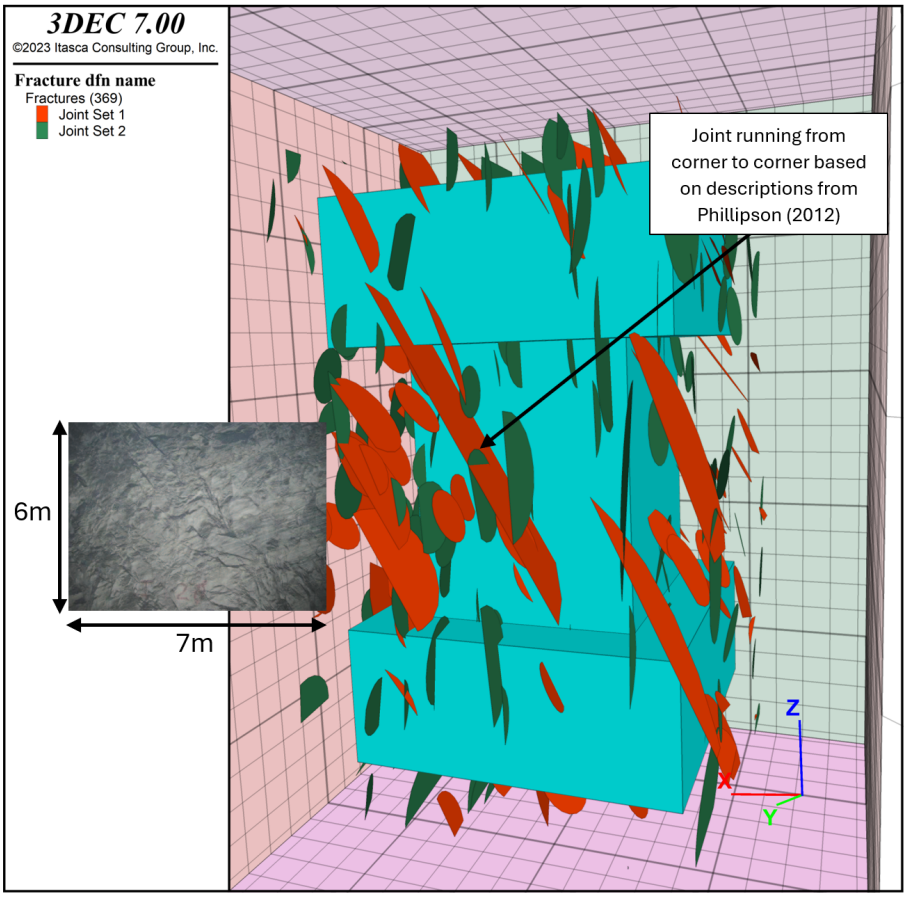

Figure 6.1: Modelled pillar with the fractures of the two joint sets. A large fracture is cross-cutting the pillar corresponding to the descriptions from Phillipson (2012). The dimensions of the left image are roughly estimated based on pillar dimensions.

The model geometry is shown in Figure 6.2a. The pillar is cut by the bedding and two discontinuity sets displayed in Figure 6.2b. These discontinuities cut the pillar into different blocks that are meshed (Figure 6.2c). The failure criteria for the discontinuities is the Mohr-Coulomb failure criteria. The pillar top is loaded with a velocity of 0.5 m/s with deformations of the pillar shown in Figure 6.2d.

Table 6.1: Model validation input parameters

Parameter	Unit	**Value**
Pillar Dimensions		
Height	m	15.24
Width	m	12.19
Intact Rock Properties		
Density	kg/m^3	2643
Young's Modulus	MPa	20.68×10^3
Poisson's Ratio		0.3
UCS	MPa	103
Tensile Strength	MPa	16.52
Cohesion	MPa	19.15
Friction Angle	°	35
Bedding Properties		
Dip	°	20
Dip Direction	°	355
Spacing	m	5
Shear Stiffness	MPa	94.25
Normal Stiffness	MPa	94.25
Friction Angle	°	30
Cohesion	MPa	1.10
Tensile Strength	MPa	0
Joint set 1 Properties		
Dip	°	65
Dip Direction	°	265
Fisher Coefficient		100
Min Length	m	2.5
Max Length	m	20
Power Law Distribution		4
Mass Density (P32)		0.1
Shear Stiffness	MPa	62.84
Normal Stiffness	MPa	62.84
Friction Angle	°	28
Cohesion	MPa	0.72
Tensile Strength	MPa	0
Joint set 2 Properties		
Dip	°	90
Dip Direction	°	265
Fisher Coefficient		100
Min Length	m	2.5
Max Length	m	20
Power Law Distribution		4
Mass Density (P32)		0.1
Shear Stiffness	MPa	94.25
Normal Stiffness	MPa	94.25
Friction Angle	°	30
Cohesion	MPa	1.10
Tensile Strength	MPa	0

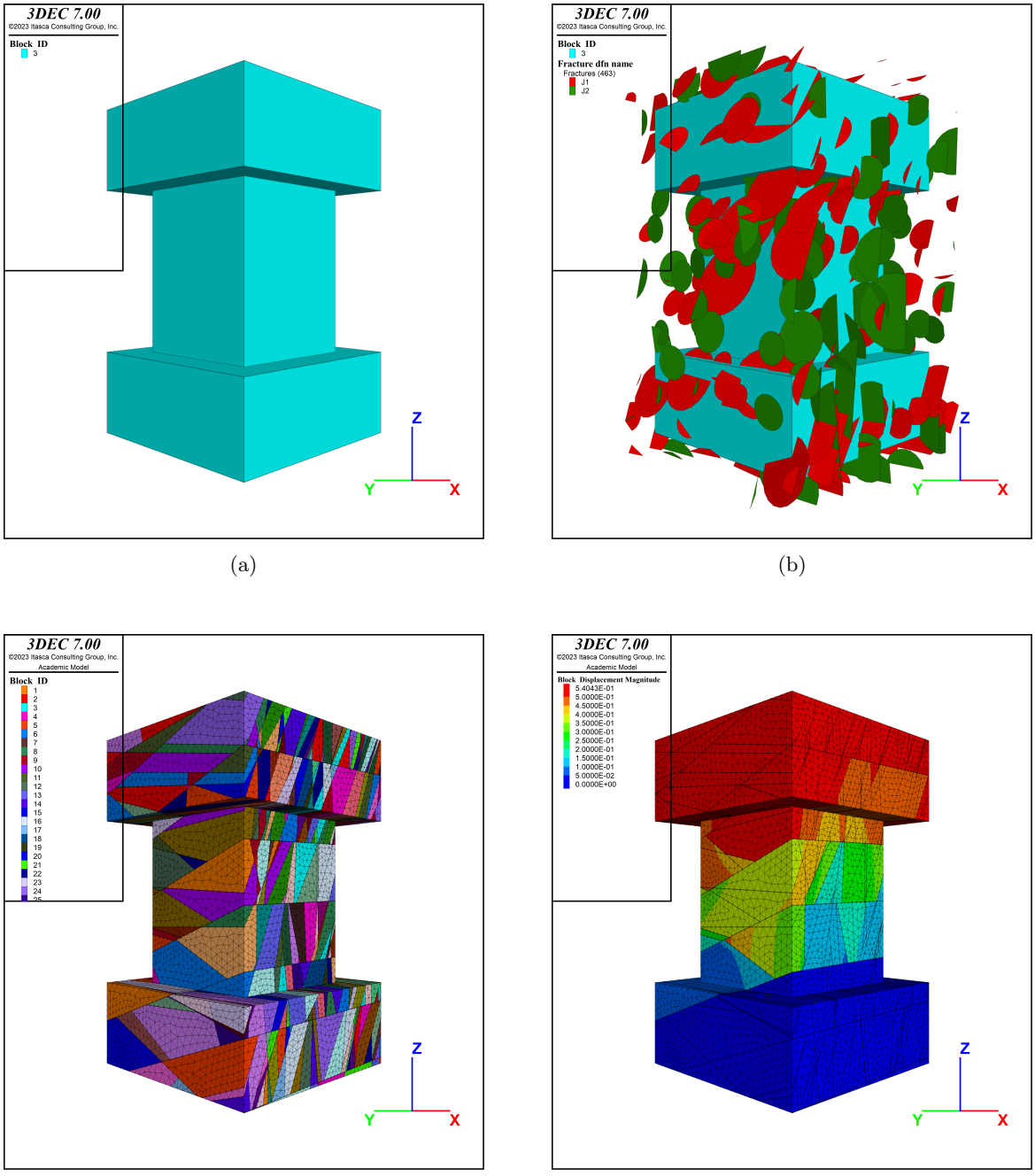

(a) (b)

(c) (d)

Figure 6.2: The process involves creating the general pillar geometry with top and bottom caps (Figure 6.2a), generating the two joint sets (Figure 6.2b) that cut the pillar with the bedding planes into distinct blocks (Figure 6.2c), and finally loading the model to observe the deformation (Figure 6.2d)

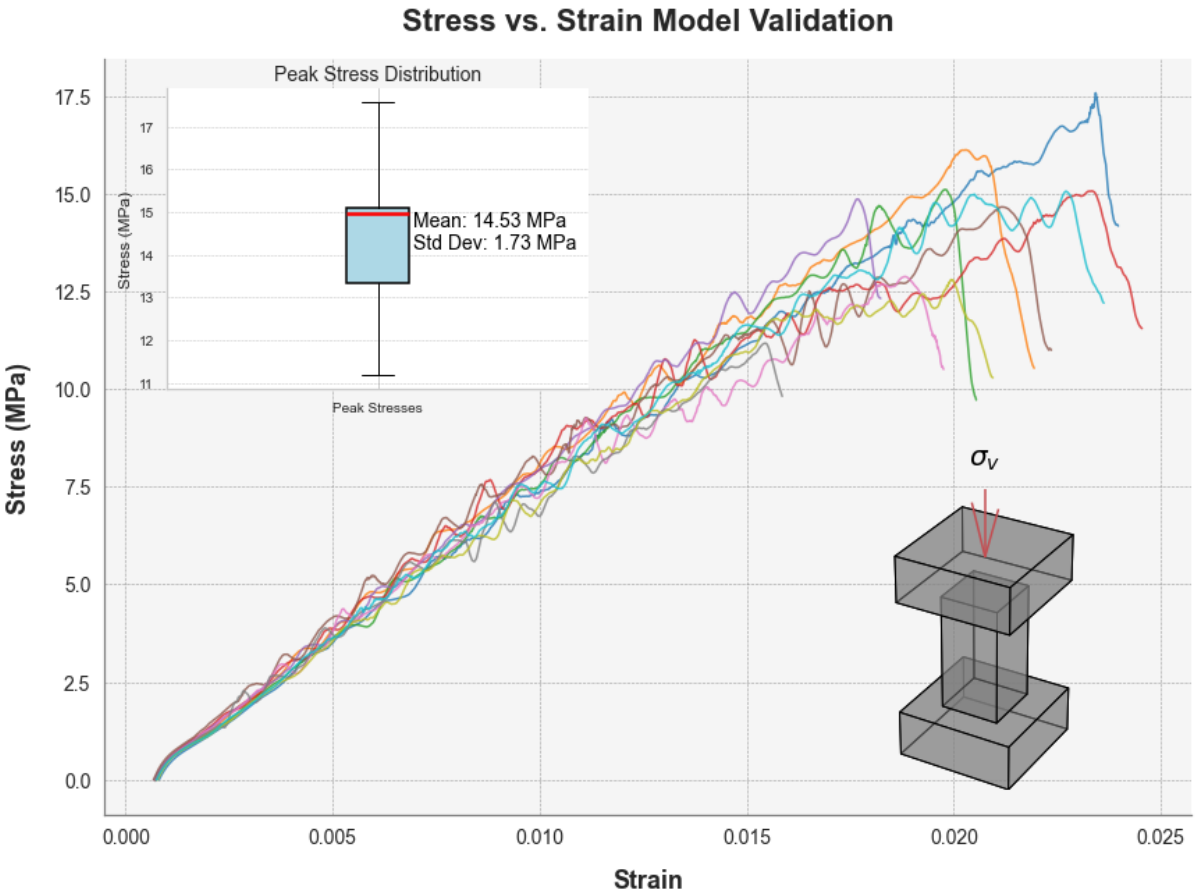

Figure 6.3: Stress-strain curves for 10 different model seeds. The box plot displays the average peak stress and the interquartile range (IQR). The standard deviation is annotated below the mean stress.

6.1.2 Results

The average pillar strength is 14.2 MPa, which is close to the expected pillar strength of 15.0 - 16.5 MPa. The average pillar stress is the average of 10 different pillar loadings for 10 different DFNs. Each DFN is varied by varying the model seed. As previously noted, this deviation is anticipated due to uncertainties in the input parameters of the DFN. The stress-strain curves show some small drops in the stress of around 1 MPa all the way up to failure, which is related to slippage along one or some discontinuities which do not result in total pillar failure. Another reason the pillar has not yet failed is that the stiffness response after the small drop in stress remains the same, meaning that the structural integrity of the pillar is still there. The total pillar failure can result in a drop in stress of around 3 MPa up to 5 MPa and is caused by slippage along one or some discontinuities that cross-cutt the pillar.

6.2 Validating Stress-Controlled Failure

To calibrate the BBM model, we simulate a UCS test performed in the laboratory with varying cohesion. The simulated UCS test result should have a strength of 182 MPa. Multiple simulations were performed with varying block contact cohesion to find the corresponding value for a UCS of 182 MPa. This cohesion of the grain boundaries is like the cohesion of the intact rock, the resistance to sliding when a shear load is applied, which does not experience normal stress. From Figure 6.4, we can see that a strength of 182 MPa corresponds to a block contact cohesion of 63 MPa. Figure 6.5 shows the model setup with the cohesion of 63 MPa.

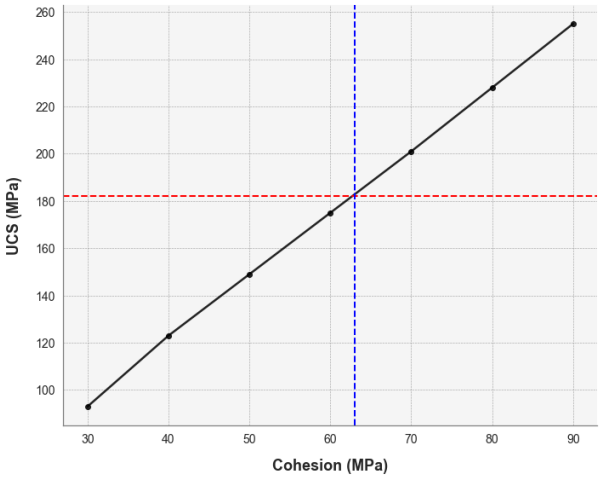

Figure 6.4: The UCS values with varying block contact cohesion.

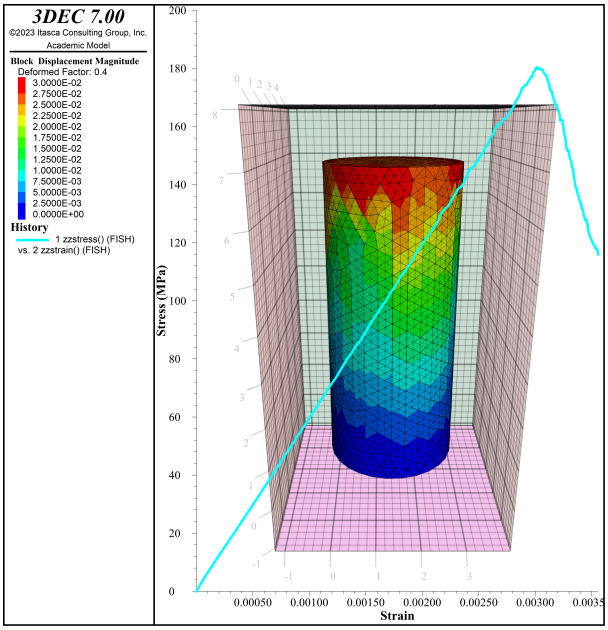

Figure 6.5: UCS test displaying the stress-strain curve and deformation in the core. The diameter is 7 m, and the height is 14 m.

7 Empirical Results: MLD Mining Dimensions

This section will review the mining dimensions determined by applying the empirical methods to the MLD rock mass. The results will show the maximum roof span for each of the four geotechnical units, accounting for variations in rock mass properties. This roof span is then used to determine the minimal pillar width, ensuring maximum recovery and stable excavation. Support measures such as shotcrete are avoided as this will significantly increase the cost of the excavation.

7.1 Roof Span

Table 7.1 shows the average Q-value determined by Jolly (2024) and the Q value accounting for the intersection. The roof span of 10 meters was chosen because increasing the roof span would put the support measures in support category 4 (Figure 5.3).

Unit	Q	Q intersection	Roof Span (m)	Roof Span Intersection (m)
S1	16	5	10	19
S2a	12	4	10	19
S2b	15	5	10	19
F	5	1.7	6	11

Table 7.1: Q values and corresponding roof spans

The minimum bolt spacing in Figure 5.3 is 1.6 m. However, for domain F, the necessary support is very close to going from support class three (systematic bolting) to support class four (systematic bolting and shotcrete, 4 - 10 cm (Figure 5.3)). Therefore, the bolt spacing of 1.5 m is used in this domain whilst it is a more conservative approach and, according to NIOSH (2011), a commonly used bolt spacing in R&P quarries. Regarding the bolt lengths, the lengths found during the empirical investigation of NIOSH (2011) vary from 0.9 m to 2.4 m. However, the larger bolt lengths determined by applying the Q-system are used to ensure a stable roof.

Unit	Q	Bolt Spacing (m)	Bolt Spacing Intersection (m)
S1	16	2.2	1.7
S2a	12	2.2	1.6
S2b	15	2.2	1.7
F	5	1.6	1.5

Table 7.2: Bolt Spacing

Unit	Q	Bolt Length (m)	Bolt Length Intersection (m)
S1	16	2.6	3.5
S2a	12	2.6	3.5
S2b	15	2.6	3.5
F	5	2.4	2.7

Table 7.3: Bolt Length

7.2 Pillar Width

As explained in Chapter 5, the pillar dimensions are calculated with a solver combining two equations (5.8 & 4.1) that meet the following criteria: FoS > 1.8, width to height > 0.8 for the given input parameters and overburden pressure. The varying input parameters are displayed in Table 7.4 with the results of the pillar width displayed in Table 7.5. For the pillar, a fixed height of 7.5 m is chosen because this is the minimum height to operate effectively, according to NIOSH (2011).

Unit	**UCS (MPa)**	**Density (kg/m^3)**	**LDF**	**DDF**	**F**	**Overburden (m)**
S1	182	2834	0.75	0.25	1	150
S2a	182	2834	0.75	0.25	1	150
S2b	182	2834	0.75	0.25	1	150
F	69	2834	0.85	0.15	1	150

Table 7.4: Input parameters for the solver

Unit	**Pillar Width (m)**	**FoS**	**Width to Height**
S1	6.3	2	0.9
S2a	6.3	2	0.9
S2b	6.3	2	0.9
F	10.5	2	1.4

Table 7.5: Results for pillar width

8 | 3DEC Results: MLD Pillar Strength

The failure after the peak stress is reached is not always similar. In some cases, the pillar loses its strength, resulting in a drop in stress. In other cases, the stress remains constant without a noticeable drop. The variations in the graphs are attributed to the different DFNs generated by varying model seeds. Therefore, the result chapter for the numerical model is divided into three sections. First, the stress-strain curves are presented, highlighting the stress-strain curves for different pillar loading with different DFNs and also displaying the average peak stress of the pillars for each distinct geotechnical unit (S1 & S2a). The second section focuses on the general failure modes observed in the pillars. Finally, the third section examines the differences between pillars that experience a significant drop in strength and those that reach their peak stress without losing strength. After these three sections, the results will be discussed in the discussion of the results.

8.1 Average Pillar Strength

8.1.1 Geotechnical Unit S1

As shown in Figure 8.1, the average pillar stress is 123 MPa, with a standard deviation of 20 MPa. Most stress-strain curves show a clear failure pattern, characterized by a noticeable drop in stress after peak load. However, some pillars maintain their strength without a significant stress drop. For this unit, seven pillars show clear failure, with three pillars maintaining their strength after failure. Another difference is the different stiffnesses of the pillars. In Section 8.3, the failure and strength behaviour of one pillar from the S1 unit is analyzed, with the observed responses attributed to the fracture orientations generated by the distinct DFN.

8.1.2 Geotechnical Unit S2a

As depicted in Figure 8.2, the average pillar stress is 140 MPa with a standard deviation of 23 MPa. For this unit, six pillars show clear failure, with four pillars maintaining their strength after failure. A difference with the S1 unit is that less stress-strain curves show a clear drop in stress. In Section 8.3, the failure and strength behaviour of one pillar from the S2a unit is also analyzed.

8.2 Failure Modes

8.2.1 Geotechnical Unit S1

Within Figure 8.3, a pillar modelled with model seed 11 of the S1 unit shows the deformation in both 3D and 2D. The difference in deformation at both sides of some of the fractures shows that sliding along this plane is taking place. Since this plane does not cross-cut the pillar from side to side, the sliding is constrained by the stiffness of the surrounding intact rock. If the fracture had fully cross-cut the pillar, it would have resulted in a total loss of pillar strength. Because this is not the case, the failure mode that will cause the pillar to lose strength is buckling due to stress-controlled failure. This buckling is visible in the 2D cross-section by the vertical cracks that developed perpendicular to the pillar side. The stresses that build up and are released due to buckling can sometimes cause rock fragments to fly out.

8.2.2 Geotechnical Unit S2a

Figure 8.4 shows similar behaviour in the pillar as Figure 8.3. Both sliding along the discontinuities and buckling are visible, with rock fragments flying out. Rock block sliding is also apparent in this pillar but involves relatively small blocks. This sliding does not result in the pillar losing its strength.

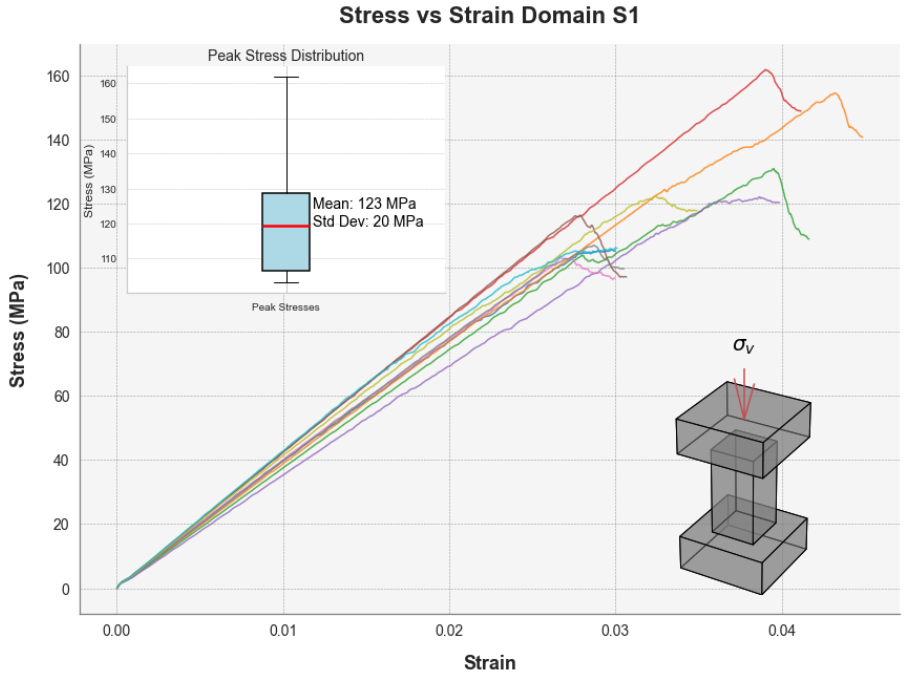

Figure 8.1: Stress-strain curves of 10 different DFNs in the S1 unit. The box plot displays the average peak stress and the interquartile range (IQR). The standard deviation is annotated below the mean stress.

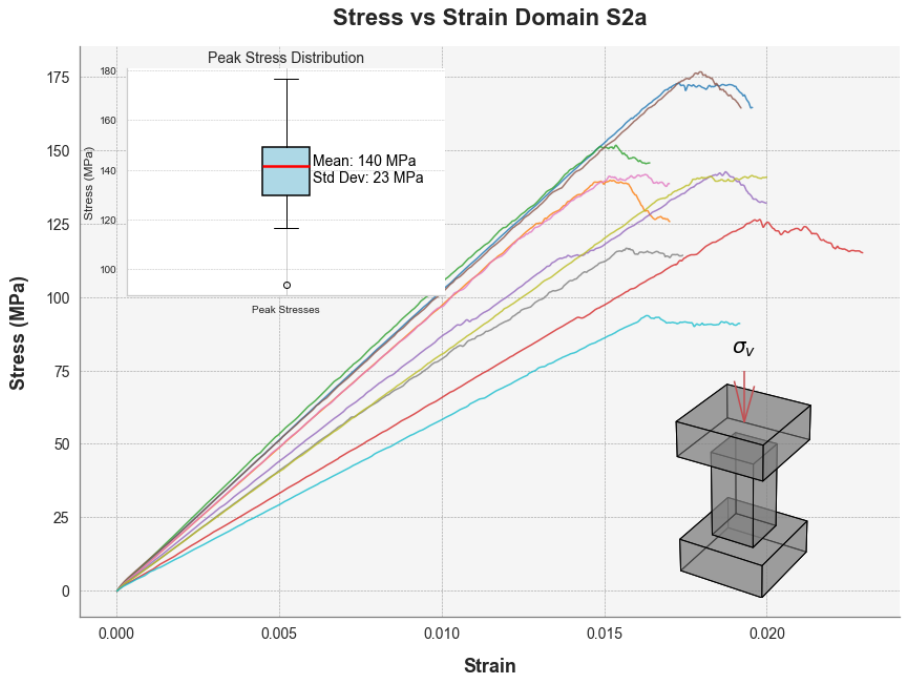

Figure 8.2: Stress-strain curves of 10 different DFNs in the S2a unit. The box plot displays the average peak stress and the interquartile range (IQR). The standard deviation is annotated below the mean stress.

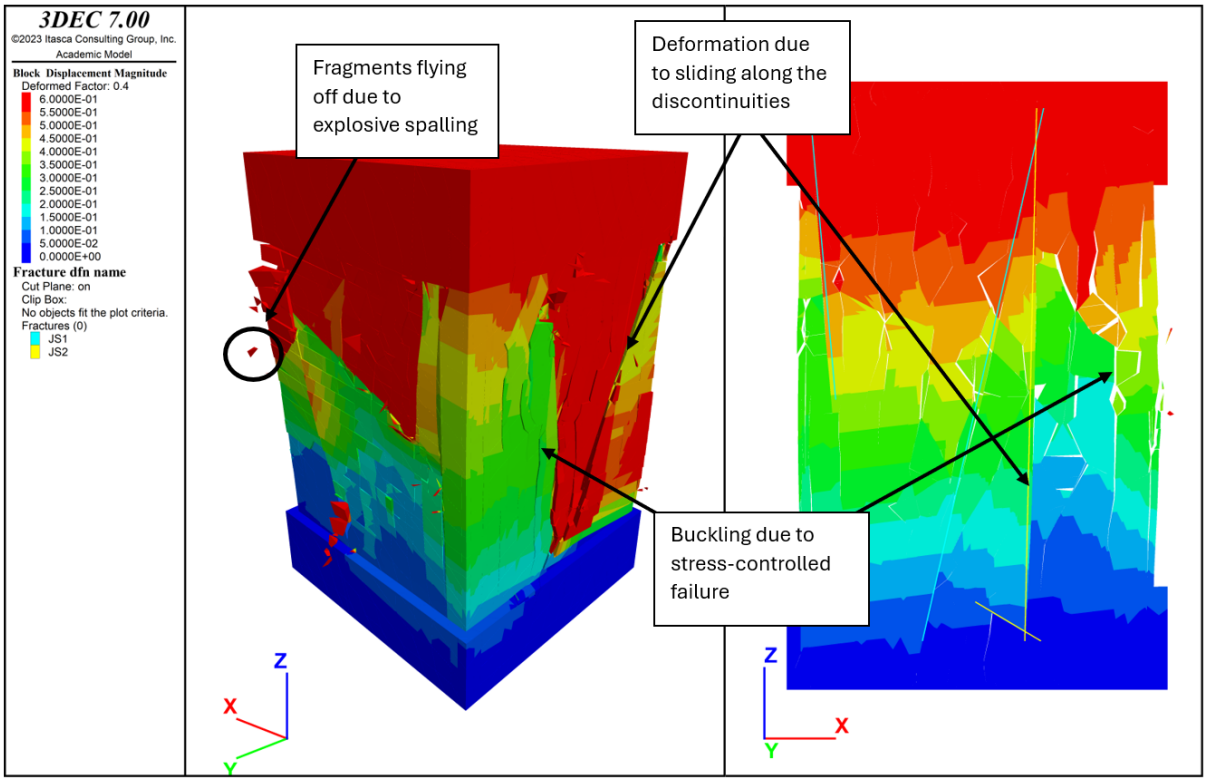

Figure 8.3: Deformation in 3D and a 2D cross-section displaying the sliding along the discontinuities and the stress-controlled failure as buckling. The DFN is created from a model seed with a value of 11 for the S1 unit.

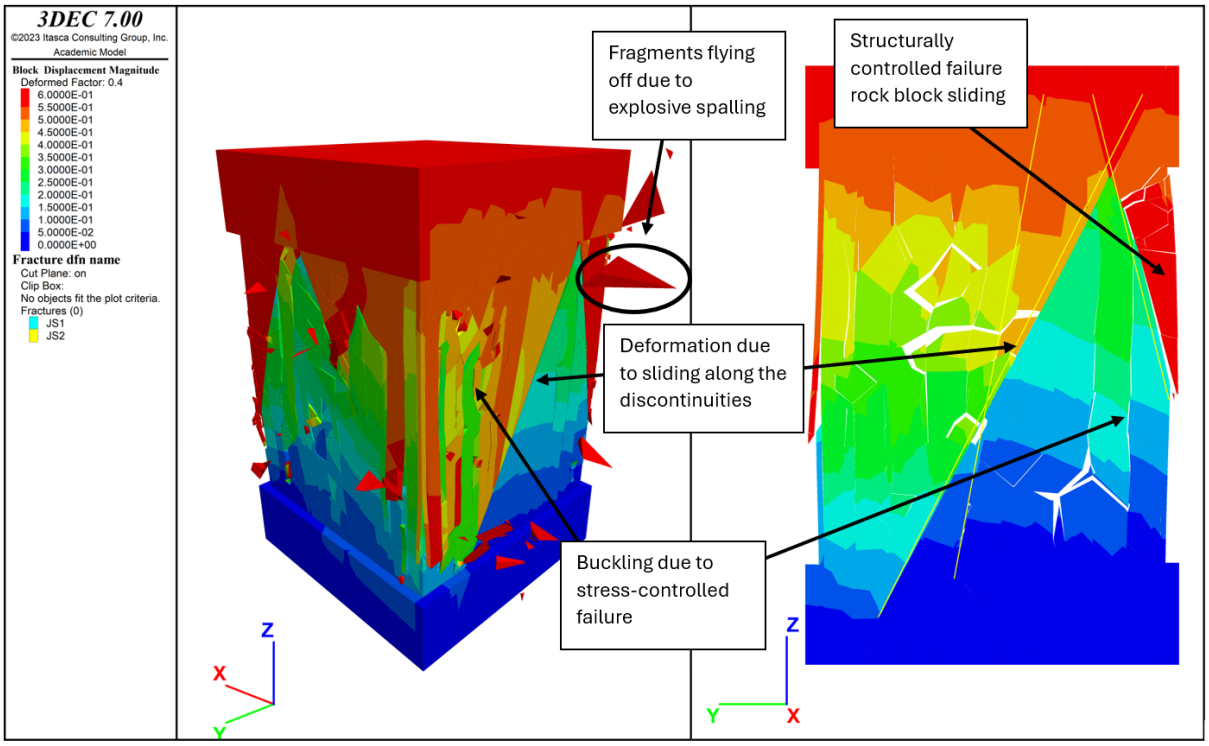

Figure 8.4: Deformation in 3D and a 2D cross-section displaying the sliding along the discontinuities and the stress-controlled failure as buckling. The DFN is created from a model seed with a value of 5 for the S2a unit.

8.3 Failure Response

When examining the different stress-strain paths, it is evident that some pillars fail and lose their strength, as indicated by a drop in stress (Figure 8.5). Other graphs show peak stress without a drop, suggesting the pillar retains its strength (Figure 8.6). The difference between these graphs is caused by the different fracture orientations and sizes from the differenet DFNs that are generated. In Figure 8.6, a fracture runs from the middle of the pillar to the side, allowing a large part of the pillar to slide outward during pillar loading. This sliding does not result in 'explosive' failure but instead causes a gradual outward sliding of this part of the pillar (shown by the black arrows). In Figure 8.5, the large fracture in the middle does not extend from the middle to the side, preventing the side block from sliding outward. Instead, it compresses, leading to buckling. This buckling eventually causes explosive failure (depicted by the black arrows). This failure is reflected in the clear drop in stress in the stress-strain graph. This pillar's peak strength is also higher than the pillar in Figure 8.6. This is because a large part of the pillar in Figure 8.6 is not fully taking on the vertical load, reducing the pillar strength.

8.4 Discussion of the Results

The bounded block model (BBM) shows good results in simulating the expected failure modes. Buckling is clearly visible in both Figures 8.3 and 8.4 just as the small rock block sliding at the sides of the pillars. Additionally, the variations in the stress-strain curves can be attributed to different fractures generated by varying DFNs. This can lead to significant differences in strength, highlighting the importance of performing a stochastic analysis. However, a significant downside is that BBM models are computationally intensive, with loading one pillar to failure could take over 15 hours. This means that computational time must be considered when applying this model setup.

Although the failure modes and strength variations between the pillars are well-modelled and clearly visible, the average pillar stress is much higher than predicted by the pillar strength equation from NIOSH (2011). According to their pillar strength equation (Equation 5.8), the pillar strength of the S1 and S2a units should be 34 MPa. The numerical model calculated an average strength of 129 MPa and 142 MPa, respectively. This is explained by the small heterogeneities such as cracks, voids, and other weaknesses that influence the intact rock, which is not considered in the numerical model. When cores are selected for testing, cracks and voids are avoided to assess the intact rock strength. Therefore, using the lab data for the pillar's intact rock properties assumes homogeneous intact rock properties which results in extremely high pillar strengths, as these small weak parts are disregarded. Especially at a larger scale, more of these weaknesses are present in the rock, decreasing the average strength of the intact rock. Therefore, calibrating the BBM is crucial to achieving realistic pillar behaviour and not directly applying the results from the lab tests. However, calibration of a model for preliminary mine design can be very difficult. Another approach is not modelling the intact rock properties of the pillar as homogeneous as was done in this research. Lavoie et al. (2022) modelled the intact rock by varying the strength of the contact of the BBM blocks. They obtained this heterogeneity by performing systematic point load tests on cores and, therefore, also including the weaker material that consisted of veins and defects. Whilst this method will result in lower pillar strength, validation is still required to determine the model's correct workings.

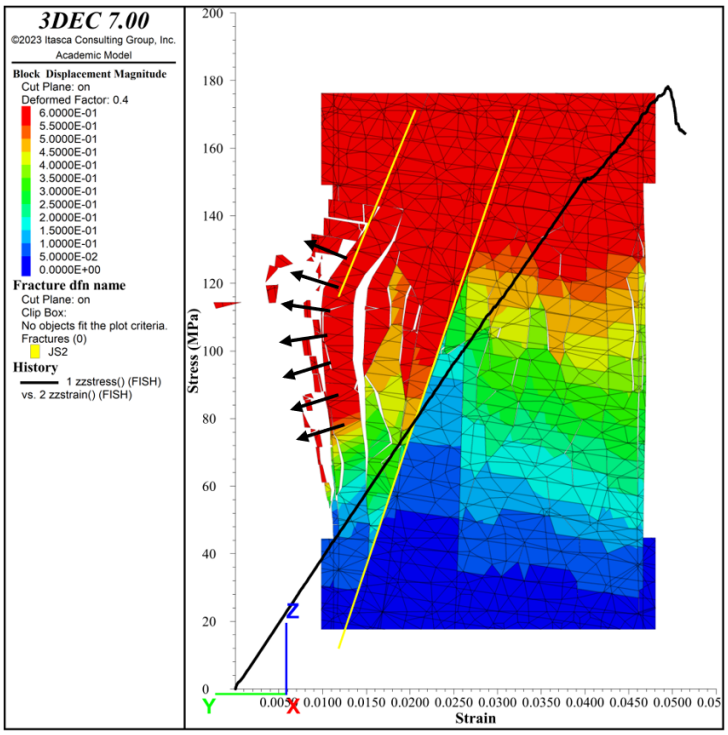

Figure 8.5: The stress-strain curve shows the peak pillar strength with a drop in stress. The black arrows show that the buckling results in breaking and explosive failure at the side of the pillar.

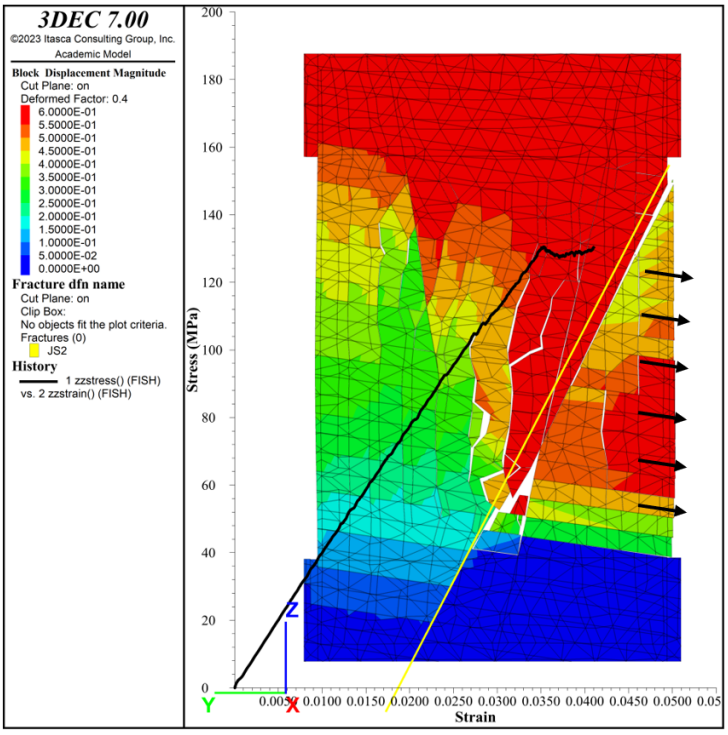

Figure 8.6: The stress-strain curve shows the peak pillar strength but does not have a significant drop in stress. The black arrows show the displacement of a part at the side of the pillar caused by a fracture of the J2 set.

9 Discussion

This discussion chapter will discuss how the findings in the results can be used in the context of R&P mining and the MLD quarry. It begins by examining the model setup used for validating structurally controlled failure and analyzing the effectiveness of this approach. Next, it addresses the challenges encountered in modelling roof stability, which has been tried in this research but was unsuccessful. Following this, a comparison between empirical and numerical methods is made, emphasizing the strengths and limitations of each for preliminary mine design and the MLD quarry in specific. The chapter concludes with recommendations for future research.

9.1 DEM model with zoned blocks

The model used for validating the structurally controlled failure was a model with zoned blocks modelled elastoplastic with infinite yield strength. The blocks can deform but cannot break as with a bounded block model (BBM). When using such a model, it is crucial to know the pillar will be subjected to structurally controlled failure and that the fractures create joint planes in 3DEC that allow sliding. To understand the latter, it is essential to understand the fracture generation process in 3DEC. Figure 9.1 illustrates that a fracture (shown in blue in the left box) cannot be modelled as a circular fracture but is part of a larger joint plane that ends when in contact with another joint or the face of a block. Only the nodes within the fracture (red nodes) are assigned fracture properties, while the surrounding nodes (green nodes) are given different properties. In this model, green nodes are assigned intact rock properties, simulating the intact rock strength along this plane. It's important to note that the blocks themselves cannot fail in this manner due to their constitutive model. Consequently, this model assumes a plane of failure with the same orientation as the distinct fractures.

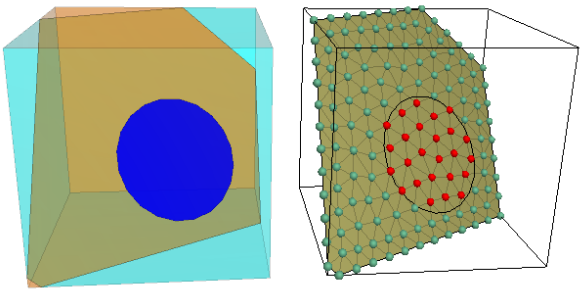

Figure 9.1: An illustration of the sub-contacts on a joint plane: red for those inside a circular fracture and green for those outside the fracture

The model validation has displayed that this model setup can produce good results in predicting the pillar strength. However, only knowing the pillar will be subjected to structurally controlled failure is not sufficient to apply this model setup. Figure 9.2 presents four images illustrating two different fracture sizes (diameter 2 m & 0.5 m) with two different bedding thicknesses (spacing 2 m & 0.2 m). It is important to note that these images do not represent pillar loadings from the MLD rock mass but are used to demonstrate a particular process in 3DEC. As shown, the joint planes (visible as orange planes) in Figures 9.2a and 9.2c are larger compared to those in Figures 9.2b and 9.2d. This is because when the fracture is generated, the joint plane has to extend to another plane or side of a block. In the two models with the thinner bedding, this joint plane does not have to extend far behind the fracture plane to be in contact with another plane. Therefore, the joint planes in these models are smaller. The larger joint planes span from one side of the pillar to the other, which allows sliding along these planes when the pillar is loaded, ultimately leading to total pillar failure seen in the stress-strain curves within Figures 9.2a & 9.2c. As expected, the peak stress of the pillar with the larger fracture is lower (70 MPa) than the pillar with the smaller fracture (135 MPa). Conversely, the models with thinner bedding do not show pillar failure, as sliding along this plane is not possible because it does not extend to the edges of the pillar. The stress-strain curves show in both models a small drop in stress, which is attributed to the failure of the joint plane but, as explained, does not result in total pillar failure. This small drop occurs for the larger fracture, around 40 MPa, and for the smaller fracture, around 140 MPa.

In practice, it is expected that both fractures of Figure 9.2a & 9.2b would result in structurally controlled failure because of the fracture almost running from side to side of the pillar. However, as demonstrated, this is not the case for the model with thin bedding. Also, the fracture in Figure 9.2c would most probably not cause failure in real life but does with this model setup. Therefore, it is crucial to understand this process as purely predicting that structurally controlled failure would happen in real life is insufficient to use this model setup. A way to circumvent this problem for 9.2b is by first cutting the model with the DFNs and afterwards by the bedding plane. However, this approach causes problems for smaller fractures again, as they will be able to fail as in Figure 9.2c.

9.2 DEM modeling roof stability

Monsalve (2019) used a DFN incorporated into a DEM to model structurally controlled roof failure in an underground excavation. The DFN was created from data from LiDAR scans, and a stochastic analysis was performed to determine whether any structurally controlled failure would occur. The blocks in the model were modelled as rigid. The underground excavation was modelled without in situ stress, which was substantiated by the fact that the horizontal stress was not high enough to induce failure. Whilst this is correct, the in situ stress does affect the stability of the roof. The maximum shear strength of a joint depends on the normal stress as displayed in Equation 9.1 (Barton, 1976). Therefore, horizontal stress might not cause blocks to break or deform but could increase normal stress and, consequently, the maximum shear stress, enhancing the roof's stability.

$$\tau = \sigma_n \tan(\phi) \tag{9.1}$$

However, the combination of in situ stress and thin bedding was found to be problematic. The roof, floor, and sides of the pillar exhibited extreme deformation. The bedding planes of the floor 'jumped' up, and the sides of the pillar were pushed inward. This likely resulted from stress changes in the rock mass following the excavation around the support pillars. 3DEC version 7 does not allow for stress relaxation at the faces of an excavation. Therefore, the removal of the excavated material abruptly increases the mechanical ratio of the model. This shock, combined with the relatively thin beds, causes rock blocks to fly into the excavated area. Various damping modes, such as 'Global' damping, were attempted to mitigate this 'shock' quickly, but none were successful. Modelling the blocks as rigid, as was the case in Monsalve (2019), will prevent this. This is because the only deformation will be attributed to the bedding planes and joints deforming due to decompression. While this approach could prevent the 'shock' through the model, incorporating in situ stress and using deformable blocks to model post-excavation deformation is crucial to modelling the effect of rock bolts on the roof stability (Peter et al., 2022). Because rock bolts are required for the underground excavation, this simplification is not possible.

9.3 Empirical and numerical methods compared

To answer whether numerical models can be used in preliminary mine design compared to empirical methods, it is essential to understand both methods' main advantages and disadvantages. The advantage of empirical methods lies in their ease of use due to a relatively low number of input parameters—such as the six parameters used in both the Q-System and the pillar strength equation from NIOSH (2011). This allows for straightforward application, as it avoids determining a wide range of parameters necessary for the numerical model. However, giving correct values to these parameters can be difficult and sometimes requires experience. For example, multiplying the J_n by three to account for tunnel intersections (as recommended by (NGI, 2022)) can be arbitrary. Also, selecting the joint conditions (Jr/Ja) is not always straightforward, as NGI (2022) suggests that the joint set most likely to slide should be selected. This prediction can be difficult in a rock mass with multiple discontinuity sets with varying orientations. This is a part where the numerical model exceeds as it allows the modelling of all the different joint sets with their strength and variations in the intact rock strength. However, with this comes a large number of input parameters increasing with each joint set added to the model. These parameters are often difficult to measure, necessitating model calibration. Unless monitoring data for model calibration is available on the rock mass, the results will be difficult to trust. And because this data is often unavailable when performing a preliminary mine design for an underground operation, the use of numerical modelling in this application is not advised. What could be done when wanting to determine the effect of certain features on the pillar strength that are not incorporated into the empirical method is calibrating the model with the results from the empirical method.

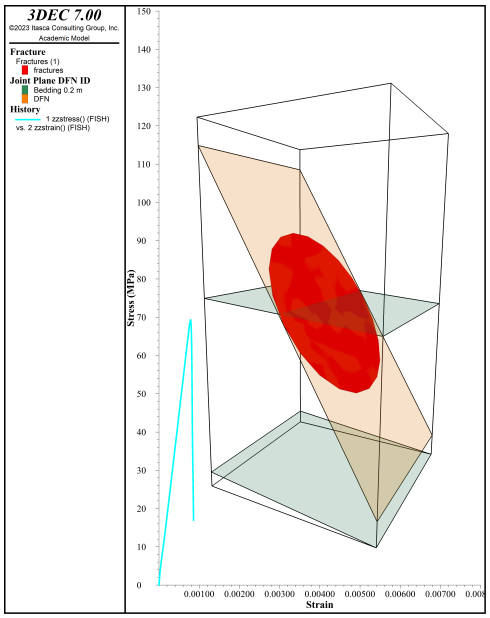

(a) Fracture diameter: 2 m, bedding spacing: 2 m

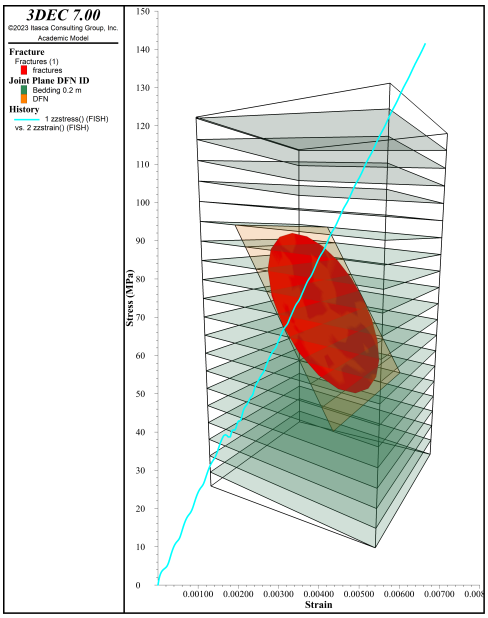

(b) Fracture diameter: 2 m, bedding spacing: 0.2 m

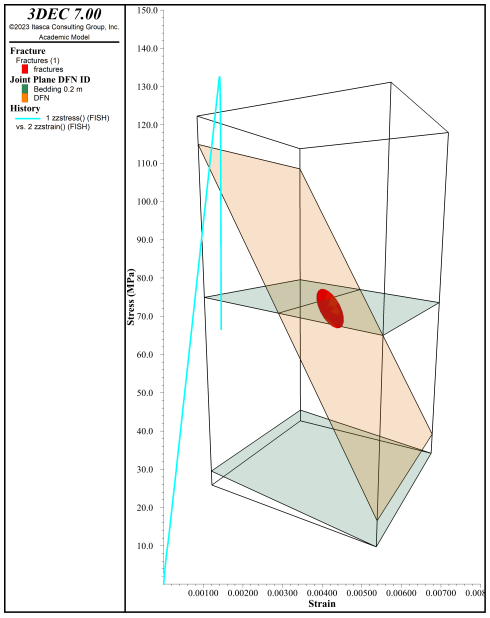

(c) Fracture diameter: 0.5 m, bedding spacing: 2.0 m

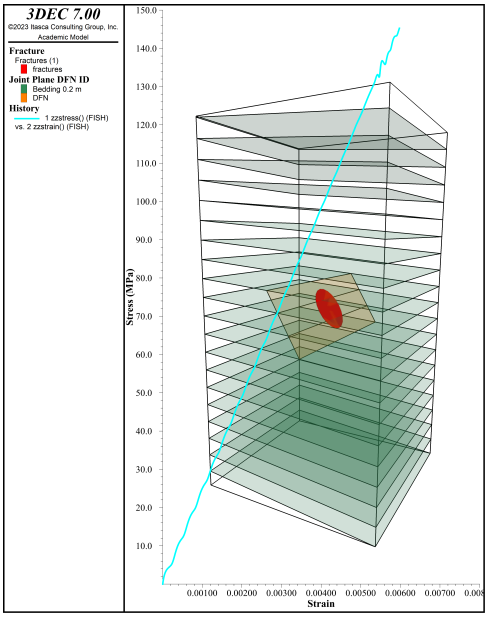

(d) Fracture diameter: 0.5 m, bedding spacing: 0.2 m

Figure 9.2: Displaying the effect of different fracture seizes and bedding thicknesses for a model that has zoned blocks that are modelled elastoplastic with infinite yield strength and joint plane properties that are assigned intact rock properties (orange plane) outside the fracture (red plane)

Contrary to the BBM model used to determine the pillar strength at the MLD quarry, the model used to validate the structurally controlled failure showed very good results in predicting the average peak strength of the pillar. Another advantage of this type of model is that the computational time is much lower, whilst it does not necessitate the subdivision of the zoned blocks into individual blocks which creates a finer mesh. Therefore, researching the effect of certain weaknesses in the pillar, such as karst voids or dissolution joints, is more practical as the computational time is not that high with this model.

For determining the R&P dimensions in the MLD quarry, it is not advised to use a DEM model to help with determining the pillar dimensions. As described, the stress-controlled failure that is expected in the MLD quarry necessitates the need for a BBM when wanting to observe the buckling of the pillar. This model has proven to overestimate the pillar strength as data to calibrate the BBM model was unavailable. The model is expected to be useful for determining the roof's stability, specifically by researching efficient rock bolting patterns. Whilst this has not worked in this research, new 3DEC features such as stress relaxation are thought to resolve most problems when modelling the underground excavation.

9.4 Recommendations

To better compare the empirical strength equation from NIOSH (2011) to 3DEC, it is suggested to create fictive data for the 3DEC input parameters. This allows a parameter sensitivity analysis whilst creating pillar geometries with DFNs that are computationally less intensive than the 3DEC model for the MLD pillar loading. There are rock mass properties that the pillar strength equation can incorporate, such as the discontinuity dip angle, discontinuity density, and the pillar width-to-height ratio. These parameters are assigned a value to reduce the pillar strength. It is suggested to first start testing these values using 3DEC in combination with a DFN. Afterwards, the effect of parameters not incorporated into the equation, such as the discontinuity friction angle, stiffness properties and the orientation of different discontinuity sets relative to each other, should be investigated. For these parameters, it is essential to use values which fall within the range of the specific sites studied in the research..

Jolly (2024) divided the fractures in the MLD quarry into structural and background joints. A study to validate this subdivision is recommended, as this research highlights the importance of incorporating weaknesses in the intact rock to avoid overestimating pillar strength. Whilst the weaknesses in the intact rock are not considered the same as background joints from a joint set, they could still affect the pillar strength. Modelling the pillar in 3DEC with and without background joints and loading the pillar until failure will provide insight into the effect these background joints have on the pillar strength. This can then justify or disprove the subdivision of these joints.

Given the occurrence of karstic features in the MLD quarry, it may be useful to investigate the strength of pillars affected by such features, similar to the approach in Soni et al. (2022). However, to investigate this, the BBM has to be improved. To achieve this, a systematic method must be developed to assess the strength of the intact rock, taking into account inherent weaknesses to better approach the real strength of the pillar. The cores in MLD have shown incomplete recovery due to material loss during coring (Jolly, 2024), introducing bias by not taking into account these weaker rocks. Therefore, an alternative method to that used by Lavoie et al. (2022), who performed systematic point load tests on cores, must be developed. An option is to establish a correlation between index tests, such as the Schmidt Hammer and UCS tests. While such a correlation had already been established during laboratory work (Jolly & Oostman, 2023), the correlation was only for unweathered material. When a good correlation is established for the full range of intact rock strengths, the rock face can be systematically tested using the Schmidt Hammer. This gives a data set that better represents the variation in the intact rock strength, which is crucial for a more realistic approximation of the strength of the intact rock as outlined in section 8.4.

Damping within the 3DEC model is crucial for producing realistic results. To equilibrate the model, 'Global' damping is applied to dissipate vibrational energy under static conditions, while 'Combined' damping is used during loading, as recommended by Sinha et al. (2022). The correct damping is particularly important in dynamic models because excessive damping can make the pillar behave more viscous,

leading to resistance to deform and overestimating the pillar's strength. A model with too much damping would show different pillar strengths for different loading rates. This is because such a pillar prevents deformation due to the resistance of deformation, which is made more pronounced at higher loading rates. The accuracy of the damping in this research was confirmed when varying loading velocities did not affect the pillar strength. Therefore, the combination of a 0.5 m/s loading rate and 'combined' damping yielded reliable results. However, further research into the effects of these parameters could provide valuable insights. The default value of the 'combined' damping mode is set at 0.8 but can be adjusted. A parameter sensitivity analysis on the damping mode and loading velocity for different pillar geometries, DFNs, and bedding planes could help better understand these parameters for future studies that use 3DEC for pillar strength determination.

10 Conclusion

Both the Q-system and R&P design guidelines from NIOSH (2011) proved effective in determining R&P mining dimensions because of its straightforward application. The maximum roof span and minimum pillar dimensions were calculated in that order to ensure the most stable excavation. The roof span was established as 10 m for the S1, S2a, and S2b units, and 6 m for the more weathered F unit with both using different rock bolting patterns. The pillar widths were 6.3 m for the first three units and 10.5 m for the F unit.

The 3DEC model allowed us to examine the failure modes in the pillar and revealed variations in pillar strength across each unit, taking into account the different fractures generated by the DFNs. However, the model did not yield reliable pillar strength results. The pillar strength was much higher than expected. According to their pillar strength equation (Equation 5.8), the pillar strength of the S1 and S2a units should be 34 MPa. The numerical model determined an average strength of 129 MPa and 142 MPa, respectively. This difference was likely due to the assumption of homogeneous intact rock properties using the average values of the laboratory tests. If possible, the bounded block model (BBM) contact parameters should be calibrated to account for weaknesses in the rock, ensuring a realistic strength at a large (pillar) scale. Without calibration, the rock properties should be modelled heterogeneously, with distribution data covering the full range of its properties, such as veins and defects. This data was unavailable, so the pillar strength results were too high and unreliable.

However, the model used to validate structurally controlled failure, which consisted of zoned blocks modelled elastoplastic with infinite yield strength, performed well in predicting the average peak pillar strength. Unlike the BBM model, this approach had lower computational time, making it more suitable for studying the effect of multiple weaknesses such as karst voids or dissolution joints. However, when employing this model setup, it is crucial to know that the pillar is subjected to structurally controlled failure and that the 3DEC fracture generation process is understood to prevent unrealistic results.

In summary, using 3DEC with integrated DFNs to determine R&P mining dimensions in the MLD quarry is not recommended. Modelling stress-controlled failure required the use of a BBM model, which was problematic due to the inability to calibrate block contacts and the lack of sufficient data to create a realistic distribution of intact rock properties. It is therefore advised to use the Q-system and R&P design guidelines from NIOSH (2011) as the results are clear, practical, and based on well-established empirical data. However, if such an operation were to happen, the numerical method could help quantify the effect of certain features on the pillar strength given that the model is well calibrated and provides realistic results.

Bibliography

Bahrani, N., & Valley, B. (2020). Three-dimensional numerical simulation of drilling-induced core damage using bonded block model.

Bandis, S. C., Lumsdent, A. C., & Barton, N. R. (1983). *Fundamentals of Rock Joint Deformation* (tech. rep. No. 6). https://www.researchgate.net/publication/321878738

Barton, N. (1976). The shear strength of rock and rock joints. *International Journal of Rock Mechanics and Mining Sciences & Geomechanics Abstracts*, *13*(9), 255–279. https://doi.org/10.1016/0148-9062(76)90003-6

Barton, N. (2013). Shear strength criteria for rock, rock joints, rockfill and rock masses: Problems and some solutions. *Journal of Rock Mechanics and Geotechnical Engineering*, *5*(4), 249–261. https://doi.org/10.1016/j.jrmge.2013.05.008

Barton, N., Lien, R., & Lunde, J. (1974). Engineering Classification of Rock Masses for the Design of Tunnel Support. *Rock Mechanics*, *6*, 13.

Barton, N. (2022). Continuum or Discontinuum - That is the question.

Bless, M. J. M., Bouckaert, J., & Paproth, E. (1983). Recent Exploration in Pre-Permian Rocks Around the Brabant Massif in Belgium, The Netherlands and The Federal Republic of Germany. *The Netherlands and the Federal Republic of Germany. Geol. Mijnbouw*, 51–62.

block mechanical command — 3DEC 7.0 documentation. (2019). https://docs.itascacg.com/3dec700/3dec/block/doc/manual/block_manual/block_commands/block/cmd_block.mechanical.html

Bonded Block Model in 3DEC. (2024). https://www.itasca.se/en/software/new-in-3dec-3

Cundal, P., & Strack, O. (1979). A Discrete Numerical Model for Granular Assemblies. *Geotechnique*, *29*(1).

Cundall, P. A. (1971). The measurement and analysis of accelerations in rock slopes. *Imperial College London*.

Esterhuizen, G., Bajpayee, T., Ellenberger, J., & Murphy, M. (2013). Practical estimation of rock properties for modeling bedded coalmine strata using the Coal Mine Roof Rating. *Geomechanics Symposium*.

Esterhuizen, G., Tyrna, P., & Murphy, M. (2019). A Case Study of the Collapse of Slender Pillars Affected by Through-Going Discontinuities at a Limestone Mine in Pennsylvania. *Rock Mechanics and Rock Engineering*, *52*(12), 4941–4952. https://doi.org/10.1007/s00603-019-01959-6

Galvin, J. (2016). *Ground Engineering - Principles and Practices for Underground Coal Mining*. Springer International Publishing. https://doi.org/10.1007/978-3-319-25005-2

Hoek, E. (1977). Structurally Controlled Instability In Underground Excavations.

Introduction — 3DEC 7.0 documentation. (2014). https://docs.itascacg.com/3dec700/3dec/docproject/source/modeling/introduction/introduction.html?node1963

ISRM. (2007). The Complete ISRM Suggested Methods for Rock Characterization, Testing and Monitoring; 1974-2006. *International Society for Rock Mechanics*. https://doi.org/10.2113/gseegeosci.15.1.47

Itasca. (2024, February). Discrete Fracture Network (DFN) Overview.

Jing, L., & Stephansson, O. (2007). Discrete Fracture Network (DFN) Method. https://doi.org/10.1016/S0165-1250(07)85010-3

Jolly, H. (2024). *Quantitative Characterization of Joint Properties in a Dolomite Deposit Using Virtual Outcrop Models, Rock Core Analysis, and Field Data for Geotechnical Applications* [Doctoral dissertation, TU Delft].

Jolly, H., & Oostman, H. (2023, October). *TUDelft lab tests on Lhoist rock samples* (tech. rep.). Delft University of Technology. Delft.

Krauland, N., & Soder, P. (1987). Determining pillar strength from pillar failure observations.

Lavoie, T., Eberhardt, E., & Pierce, M. E. (2022). Numerical modelling of rock mass bulking and geometric dilation using a bonded block modelling approach to assist in support design for deep mining pillars. *International Journal of Rock Mechanics and Mining Sciences*, *156*, 105145. https://doi.org/10.1016/j.ijrmms.2022.105145

Lei, Q., Latham, J.-P., & Tsang, C.-F. (2017). The use of discrete fracture networks for modelling coupled geomechanical and hydrological behaviour of fractured rocks. *Computers and Geotechnics*, *85*, 151–176. https://doi.org/10.1016/j.compgeo.2016.12.024

Li, A., Merifield, R., & Lyamin, A. (2008). Stability charts for rock slopes based on the Hoek–Brown failure criterion. *International Journal of Rock Mechanics and Mining Sciences*, *45*(5), 689–700. https://doi.org/10.1016/j.ijrmms.2007.08.010

Lunder, P. J. (1994). Hard rock pillar strength estimation an applied empirical approach.

Monsalve, J. J. (2019, May). *Integrating Laser Scanning with Discrete Element Modeling for Improving Safety in Underground Stone Mines* [Doctoral dissertation, Virginia Polytechnic Institute and State University].

NGI. (2022, June). *Using the Q-system*. Allkopi AS.

Nielsen, P., Swennen, R., & Keppens, E. (1994). Multiple-step recrystallization within massive ancient dolomite units: an example from the Dinantian of Belgium. *Sedimentology*, *41*(3), 567–584. https://doi.org/10.1111/j.1365-3091.1994.tb02011.x

NIOSH. (2011). *Pillar and Roof Span Design Guidelines for Underground Stone Mines* (tech. rep.). www.cdc.gov/niosh.

NIRAS. (2001, December). *Safety Assessment and Feasibility Interim Report 2* (tech. rep.). ONDRAF/NIRAS. Brussels.

Park, H., & West, T. (2002). Sampling bias of discontinuity orientation caused by linear sampling technique. *Engineering Geology*, *66*(1-2), 99–110. https://doi.org/10.1016/S0013-7952(02)00034-0

Peter, K., Moshood, O., Akinseye, P. O., Martha, A., Khadija, S. O., Abdulsalam, J., Ismail, L. A., & Emman, A. A. (2022). An Overview of the Use of Rockbolts as Support Tools in Mining Operations. *Geotechnical and Geological Engineering*, *40*(4), 1637–1661. https://doi.org/10.1007/s10706-021-02005-5

Phillipson, S. E. (2012). Massive Pillar Collapse: A Room–and–Pillar Marble Mine Case Study. *International Conference on Ground Control in Mining*.

Poty, E. (2016). The Dinantian (Mississippian) succession of southern Belgium and surrounding areas: stratigraphy improvement and inferred climate reconstruction. *Geologica Belgica*, *19*(1-2), 177–200. https://doi.org/10.20341/gb.2016.014

Robert, P. (1989). The thermal setting of Carboniferous basins in relation to the Variscan orogeny in Central and Western Europe. *International Journal of Coal Geology*, *13*(1-4), 171–206. https://doi.org/10.1016/0166-5162(89)90094-3

RS3 Program Updates. (2024, September). https://www.rocscience.com/support/rs3/release-notes

Sari, M. (2022). Two- and three-dimensional stability analysis of underground storage caverns in soft rock (Cappadocia, Turkey) by finite element method. *Journal of Mountain Science*, *19*(4), 1182–1202. https://doi.org/10.1007/s11629-021-7047-1

Sinha, S., Abousleiman, R., & Walton, G. (2022). Effect of Damping Mode in Laboratory and Field-Scale Universal Distinct Element Code (UDEC) Models. *Rock Mechanics and Rock Engineering*, *55*(5), 2899–2915. https://doi.org/10.1007/s00603-021-02609-6

Soni, A., Monsalve, J. J., Bishop, R., Ripepi, N., & Baggett, J. G. (2022, June). Estimating Strength of Pillars with Karst Voids in a Room-and-Pillar Limestone Mine. https://doi.org/10.1007/s42461-022-00594-0

Statham, I., & Treharne, G. (1991). Subsidence due to abandoned mining in the South Wales coalfield, UK: causes, mechanisms, and environmental risk assessment. *International Journal of International Association of Hydrological Sciences*, *200*, 143–152. https://doi.org/10.1016/0148-9062(92)94157-M

Suner, M. C., & Tulu, I. B. (2022). Examining the Effect of Natural Fractures on Stone Mine Pillar Strength Through Synthetic Rock Mass Approach. *Mining, Metallurgy & Exploration*, *39*(5), 1863–1871. https://doi.org/10.1007/s42461-022-00649-2

Terzaghi, R. D. (1965). Sources of Error in Joint Surveys. *Géotechnique*, *15*(3), 287–304. https://doi.org/10.1680/geot.1965.15.3.287

Tzalamarias, M., Tzalamarias, I., Benardos, A., & Marinos, V. (2019). Room and Pillar Design and Construction for Underground Coal Mining in Greece. *Geotechnical and Geological Engineering*, *37*(3), 1729–1742. https://doi.org/10.1007/s10706-018-0717-2

van der Voet, E., Laenen, B., Muchez, P., Lagrou, D., Claes, H., Verbiest, M., & Swennen, R. (2022). Controls of dolomitization and bed thickness on fracture networks in Lower Carboniferous carbonates in southern Belgium. *Journal of Structural Geology*, *164*, 104729. https://doi.org/10.1016/j.jsg.2022.104729

Vandycke, S. (1997). Post-Hercynian brittle tectonics and paleostress analysis in Carboniferous limestones. *Aardkundige Mededelingen*, *8*, 193–196.

Vasovic, A. (2024, June). Serbia's green activists rally against Rio Tinto lithium project.

11 Appendix

11.1 3DEC Code: Structurally Controlled Failure Model Validation

11.1.1 Parameters

```
def params
  pillarH               = 15.24
  pillarW               = 12.19
  brickx1               = 0
  brickx2               = 0.5*pillarW + pillarW
  brickx3               = 0.25*pillarW
  brickx4               = 0.25*pillarW + pillarW
  bricky1               = 0
  bricky2               = 0.5*pillarW + pillarW
  bricky3               = 0.25*pillarW
  bricky4               = 0.25*pillarW + pillarW
  brickz1               = 0
  brickz2               = 0.5*pillarH
  brickz3               = 0.5*pillarH + pillarH
  brickz4               = pillarH + pillarH
  extentx1              = brickx1 - 2
  extentx2              = brickx2 + 2
  extenty1              = bricky1 - 2
  extenty2              = bricky2 + 2
  extentz1              = brickz1 - 2
  extentz2              = brickz4 + 2

  ; intact rock properties
  dens                  = 2643
  young                 = 20.68e9
  poisson               = 0.3
  tension               = 16.52e6
  cohesion              = 19.15e6
  friction              = 35

  ; bedding properties
  dipB                  = 20
  ddB                   = 355
  spacingB              = 5
  stiffness_shear_B     = 94.25e6
  stiffness_normal_B    = 94.25e6
  frictionB             = 30
  cohesionB             = 1.10e6
  tensionB              = 0

  ; J1 properties
  dip1                  = 65
  dd1                   = 265
  fish1                 = 100
  lmin1                 = 2.5
  lmax1                 = 20
  lpw1                  = 4
  md1                   = 0.1
```

```
  stiffness_shear_1     = 62.84e6
  stiffness_normal_1    = 62.84e6
  friction1             = 28
  cohesion1             = 0.72e6
  tension1              = 0

  ; J2 properties
  dip2                  = 90
  dd2                   = 265
  fish2                 = 100
  lmin2                 = 2.5
  lmax2                 = 20
  lpw2                  = 4
  md2                   = 0.1
  stiffness_shear_2     = 94.25e6
  stiffness_normal_2    = 94.25e6
  friction2             = 30
  cohesion2             = 1.10e6
  tension2              = 0


  cover = 152.4
  overburden_pressure = cover * 9.81 * dens * ((2 * pillarW)^2 / pillarW^2)
  overburden_pressure_neg = overburden_pressure * -1

  TARGET = overburden_pressure * 1.1
end
```

11.1.2 Create geometry

```
model new
block tolerance 1e-5

call '00_Parameters.dat'
[params]

; define random seed
model random 1

; model domain
model domain extent ([extentx1], [extentx2]) ([extenty1], [extenty2]) ([extentz1], [extentz2])

; generate pillar dimension
block create brick ([brickx1], [brickx2]) ([bricky1], [bricky2]) ([brickz1], [brickz2])
block create brick ([brickx1], [brickx2]) ([bricky1], [bricky2]) ([brickz3], [brickz4])
block create brick ([brickx3], [brickx4]) ([bricky3], [bricky4]) ([brickz2], [brickz3])

block join

; generate Bedding
block cut joint-set dip [dipB] dip-direction [ddB] spacing [spacingB] jointset-id 2

; generate DFN
fracture template create 'J1' orientation fisher [dip1],[dd1],[fish1] ...
     size power-law [lpw1] size-limit [lmin1] [lmax1]
fracture generate dfn 'J1' generation-box ...
     -20 40 -20 40 -20 40 template 'J1' mass-density [md1]

fracture template create 'J2' orientation fisher [dip2],[dd2],[fish2] ...
     size power-law [lpw2] size-limit [lmin2] [lmax2]
fracture generate dfn 'J2' generation-box ...
     -20 40 -20 40 -20 40 template 'J2' mass-density [md2]


; cut block with the DFN
block cut dfn name 'J1'
block cut dfn name 'J2'

block zone generate-new


model save 'Validation_Geometry.sav'
```

11.1.3 Assign properties

```
model restore 'Validation_Geometry.sav'

model large-strain off
```

```
4
5  call '00_Parameters.dat'
6  [params]
7
8  ; block constitutive model and properties
9  block zone cmodel assign elastic
10 block zone prop dens [dens] young [young] poisson [poisson]
11
12
13 ; joint constitutive model and properties
14 block contact jmodel assign mohr
15
16 block contact property stiffness-normal [young] stiffness-shear [young] friction [friction] cohesion
       [cohesion] tension [tension]
17
18 block contact property stiffness-shear [stiffness_shear_B] stiffness-normal [stiffness_normal_B]
       friction [frictionB] range joint-set 2
19
20 block contact jmodel assign mohr range dfn-3dec 'J1'
21 block contact prop stiffness-shear [stiffness_shear_1] stiffness-normal [stiffness_normal_1]
       friction [friction1] range dfn-3dec 'J1'
22
23 block contact jmodel assign mohr range dfn-3dec 'J2'
24 block contact prop stiffness-shear [stiffness_shear_2] stiffness-normal [stiffness_normal_2]
       friction [friction2] range dfn-3dec 'J2'
25
26 block contact material-table default prop stiffness-shear [stiffness_shear_1] stiffness-normal
       [stiffness_normal_1] friction [friction1] cohesion 0 tension 0
27
28
29 ; gravity
30 model gravity = 0, 0, -9.81
31
32 ; overburden pressure
33 ;block insitu topo ratio-x 0.5 ratio-y 0.5 overburden [overburden_pressure_neg]
34 ;block face apply stress-zz  [overburden_pressure_neg] range pos-z [brickz4]
35
36 ; boundary conditions
37 block gridpoint apply velocity-x 0 velocity-y 0 velocity-z 0 range position-z [brickz1]
38 block gridpoint apply velocity-x 0 range position-x [brickx1]
39 block gridpoint apply velocity-x 0 range position-x [brickx2]
40 block gridpoint apply velocity-y 0 range position-y [bricky1]
41 block gridpoint apply velocity-y 0 range position-y [bricky2]
42
43 ; apply damping
44 block mechanical damping global
45
46 ; keep track of mechanical ratio
47 model history mechanical ratio
48
49 block gridpoint group 'top' range pos-z [brickz4]
50 block gridpoint group 'bottom' range pos-z [brickz1]
51
52 ; equilibrate with high values of joint cohesion and tension
53 model solve
54
55 ; assign the realistic joint cohesion and tension
56 block contact prop cohesion 1.1e6 tension 0 range joint-set 2
57 block contact prop cohesion 0.7e6 tension 0 range dfn-3dec 'J1'
58 block contact prop cohesion 1.1e6 tension 0 range dfn-3dec 'J2'
59
60 ; equilibrate model
61 model solve
62
63 model save 'Validation_Equilibrium.dat'
```

11.1.4 Pillar loading

```
1      model restore 'Validation_Equilibrium.dat'
2
3  block mechanical damping local 0.1
4  ;block mechanical damping combined
5
6  [global area = pillarW^2]
7  [global length = 2*pillarH]
8
9  fish def zzstress
10   ; compression positive, units MPa
11   local top_reaction = 0.0
12   loop foreach gp block.gp.list
13     if block.gp.group(gp) = 'top'
14       top_reaction = top_reaction - block.gp.force.reaction.z(gp)
```

```
      local top_disp = block.gp.disp.z(gp)
    endif
  end_loop

  zzstress = 1e-6*top_reaction/area
  zzstrain = -1*top_disp/length
end

fish history zzstress
fish history zzstrain

; define certain model
block history velocity-z position [pillarW] [pillarW] [brickz4]
model history mechanical ratio

fish def params_shear
  global zvel_=-0.5
end
[params_shear]

[global cyc0 = mech.cycle]

; velocity ramp with shape of CDF
fish def ramp
  ramp = 1 / (1 + math.exp(-0.001 * ((mech.cycle - cyc0) - 10000)))
end

block gridpoint apply vel-z [zvel_] fish ramp range group 'top'

model cycle 20000


block gridpoint apply-remove vel-z range group 'top'

block gridpoint apply velocity-z [zvel_] range group 'top'

model cycle 40000

model save 'Pillar_Loading.dat'
```

11.2 3DEC Code: Stress Controlled Failure Model Validation & Pillar Loading Empirically Determined Dimensions

11.2.1 Parameters

```
def paramUCS
  pillarH               = 7 * 2.3
  pillarW               = 2.658680776 * 2.3
  brickx1               = 0
  brickx2               = 0.5 + pillarW
  brickx3               = 0.25
  brickx4               = 0.25 + pillarW
  bricky1               = 0
  bricky2               = 0.5 + pillarW
  bricky3               = 0.25
  bricky4               = 0.25 + pillarW
  extentx1              = brickx1 - 2
  extentx2              = brickx2 + 2
  extenty1              = bricky1 - 2
  extenty2              = bricky2 + 2
  extentz1              = 0 - 2
  extentz2              = pillarH + 2

  dens                  = 2834
  young                 = 67.6E9
  poisson               = 0.22
  tension               = 11e6
  cohesion              = 63e6
  friction              = 49.39

  cover                 = 150
  overburden_pressure   = cover * 9.81 * dens * ((2 * pillarW)^2 / pillarW^2)
  overburden_pressure_neg = overburden_pressure * -1
  FoS                   = 2
  TARGET = overburden_pressure * FoS
end

def paramS1_Mean
  pillarH               = 7.5
  pillarW               = 6.3
  brickx1               = 0
  brickx2               = 0.5 + pillarW
  brickx3               = 0.25
  brickx4               = 0.25 + pillarW
  bricky1               = 0
  bricky2               = 0.5 + pillarW
  bricky3               = 0.25
  bricky4               = 0.25 + pillarW
  brickz1               = 0
  brickz2               = 0.25*pillarH
  brickz3               = 0.25*pillarH + pillarH
  brickz4               = 0.5*pillarH + pillarH
  extentx1              = brickx1 - 2
  extentx2              = brickx2 + 2
  extenty1              = bricky1 - 2
  extenty2              = bricky2 + 2
  extentz1              = brickz1 - 2
  extentz2              = brickz4 + 2

  dens                  = 2834
  young                 = 67.6E9
  poisson               = 0.22
  tension               = 11e6
  cohesion              = 63e6
  friction              = 49.39

  dipB                  = 11
  ddB                   = 220
  spacingB              = 0.35;0.2 ;0.35
  stiffness_shear_B     = 29.25e9
  stiffness_normal_B    = 18.8e9
```

```
    frictionB             = 30
    cohesionB             = 0
    tensionB              = 0

    dipS1                  = 80
    ddS1                   = 300
    fishS1                 = 45
    lminS1                 = 9
    lmaxS1                 = 30
    lpwS1                  = 1.25
    mdS1                   = 0.123
    stiffness_shear_S1     = 29.25e9
    stiffness_normal_S1    = 18.8e9
    frictionS1             = 36.99
    frictionS1STD          = 13.04
    cohesionS1             = 0
    tensionS1              = 0

    dipS2                  = 80
    ddS2                   = 019
    fishS2                 = 35
    lminS2                 = 9
    lmaxS2                 = 30
    lpwS2                  = 1.25
    mdS2                   = 0.3
    stiffness_shear_S2     = 29.25e9
    stiffness_normal_S2    = 18.8e9
    frictionS2             = 33.23
    frictionS2STD          = 15.56
    cohesionS2             = 0
    tensionS2              = 0

    dipB1                  = 80
    ddB1                   = 300
    fishB1                 = 45
    lminB1                 = 1
    lmaxB1                 = 10
    lpwB1                  = 1.6
    mdB1                   = 0.19
    stiffness_shear_B1     = 29.25e9
    stiffness_normal_B1    = 18.8e9
    frictionB1             = 41.69
    frictionB1STD          = 12.85
    cohesionB1             = 0
    tensionB1              = 0

    dipB2                  = 80
    ddB2                   = 019
    fishB2                 = 35
    lminB2                 = 1
    lmaxB2                 = 10
    lpwB2                  = 1.6
    mdB2                   = 0.16
    stiffness_shear_B2     = 29.25e9
    stiffness_normal_B2    = 18.8e9
    frictionB2             = 41.69
    frictionB2STD          = 12.85
    cohesionB2             = 0
    tensionB2              = 0

    cover                 = 150
    overburden_pressure   = cover * 9.81 * dens * ((2 * pillarW)^2 / pillarW^2)
    overburden_pressure_neg = overburden_pressure * -1
    FoS                   = 2
    TARGET = overburden_pressure * FoS
  end

  def paramS2a_Mean
    pillarH               = 7.5
    pillarW               = 6.3
    brickx1               = 0
    brickx2               = 0.5 + pillarW
    brickx3               = 0.25
    brickx4               = 0.25 + pillarW
    bricky1               = 0
    bricky2               = 0.5 + pillarW
    bricky3               = 0.25
    bricky4               = 0.25 + pillarW
    brickz1               = 0
    brickz2               = 0.25*pillarH
    brickz3               = 0.25*pillarH + pillarH
    brickz4               = 0.5*pillarH + pillarH
    extentx1              = brickx1 - 2
    extentx2              = brickx2 + 2
    extenty1              = bricky1 - 2
    extenty2              = bricky2 + 2
    extentz1              = brickz1 - 2
```

```
    extentz2              = brickz4 + 2

    dens                  = 2834
    young                 = 67.6E9
    poisson               = 0.22
    tension               = 11e6
    cohesion              = 63e6
    friction              = 49.39

    dipB                  = 11
    ddB                   = 220
    spacingB              = 2.5 ;0.7 2.5 - 4
    stiffness_shear_B     = 29.25e9
    stiffness_normal_B    = 18.8e9
    frictionB             = 30
    cohesionB             = 0
    tensionB              = 0

    dipS1                  = 80
    ddS1                   = 300
    fishS1                 = 45
    lminS1                 = 9
    lmaxS1                 = 30
    lpwS1                  = 1.2
    mdS1                   = 0.24
    stiffness_shear_S1     = 29.25e9
    stiffness_normal_S1    = 18.8e9
    frictionS1             = 36.99
    frictionS1STD          = 13.04
    cohesionS1             = 0
    tensionS1              = 0

    dipS2                  = 80
    ddS2                   = 019
    fishS2                 = 35
    lminS2                 = 9
    lmaxS2                 = 30
    lpwS2                  = 1.4
    mdS2                   = 0.23
    stiffness_shear_S2     = 29.25e9
    stiffness_normal_S2    = 18.8e9
    frictionS2             = 33.23
    frictionS2STD          = 15.56
    cohesionS2             = 0
    tensionS2              = 0

    dipB1                  = 80
    ddB1                   = 300
    fishB1                 = 45
    lminB1                 = 1
    lmaxB1                 = 10
    lpwB1                  = 1.6
    mdB1                   = 0.37
    stiffness_shear_B1     = 29.25e9
    stiffness_normal_B1    = 18.8e9
    frictionB1             = 41.69
    frictionB1STD          = 12.85
    cohesionB1             = 0
    tensionB1              = 0

    dipB2                  = 80
    ddB2                   = 019
    fishB2                 = 35
    lminB2                 = 1
    lmaxB2                 = 10
    lpwB2                  = 1.4
    mdB2                   = 0.42
    stiffness_shear_B2     = 29.25e9
    stiffness_normal_B2    = 18.8e9
    frictionB2             = 41.69
    frictionB2STD          = 12.85
    cohesionB2             = 0
    tensionB2              = 0

    overburden            = 150 - 2*pillarH
    overburden_pressure = overburden * 9.81 * dens
    overburden_pressure_neg = overburden_pressure * -1
end
```

11.2.2 Create tetrahedral filled block

```
model new
```

```
2
3  block tolerance 1e-5
4
5  call '00_Parameters.dat'
6  [paramS1_Mean] ;or any other of the defined parameters
7
8  ; model domain
9  model domain extent ([extentx1], [extentx2]) ([extenty1], [extenty2]) ([extentz1], [extentz2])
10
11 ; generate pillar dimension
12 block create brick ([brickx1], [brickx2]) ([bricky1], [bricky2]) ([brickz1], [brickz4])
13
14 block zone generate edgelength 0.6
15
16 block zone list poly
```

11.2.3 Create pillar geometry and cut the pillar by the bedding and DFNs

```
1  model new
2
3  model random 2
4
5  block tolerance 1e-6
6
7  call '00_Parameters.dat'
8  [paramS1_Mean] ;or any other of the defined parameters
9
10 program call 'poly'
11
12 ; model domain
13 model domain extent ([extentx1], [extentx2]) ([extenty1], [extenty2]) ([extentz1], [extentz2])
14
15 block cut joint-set dip 0 dip-d 0 origin 0 0 [brickz2] jointset-id 99
16 block cut joint-set dip 0 dip-d 0 origin 0 0 [brickz3] jointset-id 99
17
18 block cut joint-set dip 90 dip-d 90 origin  [brickx3] 0 0 jointset-id 99
19 block cut joint-set dip 90 dip-d 90 origin [brickx4] 0 0 jointset-id 99
20 block cut joint-set dip 90 dip-d 0 origin 0 [bricky3] 0 jointset-id 99
21 block cut joint-set dip 90 dip-d 0 origin 0 [bricky4] 0 jointset-id 99
22
23 block delete range pos-z [brickz2] [brickz3] pos-x [brickx1] [brickx3]
24 block delete range pos-z [brickz2] [brickz3] pos-x [brickx4] [brickx2]
25
26 block delete range pos-z [brickz2] [brickz3] pos-y [bricky1] [bricky3]
27 block delete range pos-z [brickz2] [brickz3] pos-y [bricky4] [bricky2]
28
29
30 ; generate Bedding
31 block cut joint-set dip [dipB] dip-direction [ddB] spacing [spacingB] jointset-id 2
32
33 ; create weathered zone
34 ;block cut joint-set dip [dipwz] dip-direction [ddwz] spacing 1 number 2 ori 0 0 0
35 ;block group 'bottom' range plane dip [dipwz] dip-direction [ddwz] ori 0 0 0 distance 0.7
36 ;block delete range group 'bottom'
37
38 ; generate DFN
39 fracture template create 'JS1' orientation fisher [dipS1],[ddS1],[fishS1] ...
40      size power-law [lpwS1] size-limit [lminS1] [lmaxS1]
41 fracture generate dfn 'JS1' generation-box ...
42      0 10 0 10 0 15 template 'JS1' mass-density [mdS1]
43
44 fracture template create 'JS2' orientation fisher [dipS2],[ddS2],[fishS2] ...
45      size power-law [lpwS2] size-limit [lminS2] [lmaxS2]
46 fracture generate dfn 'JS2' generation-box ...
47      0 10 0 10 0 15 template 'JS2' mass-density [mdS2]
48
49 ;fracture template create 'JB1' orientation fisher [dipB1],[ddB1],[fishB1] ...
50 ;     size power-law [lpwB1] size-limit [lminB1] [lmaxB1]
51 ;fracture generate dfn 'JB1' generation-box ...
52 ;     0 10 0 10 0 15 template 'JB1' mass-density [mdB1]
53 ;
54 ;fracture template create 'JB2' orientation fisher [dipB2],[ddB2],[fishB2] ...
55 ;     size power-law [lpwB2] size-limit [lminB2] [lmaxB2]
56 ;fracture generate dfn 'JB2' generation-box ...
57 ;     0 10 0 10 0 15 template 'JB2' mass-density [mdB2]
58
59 ; cut block with the DFN
60 block cut dfn name 'JS1'
61 block cut dfn name 'JS2'
```

```
;block cut dfn name 'JB1'
;block cut dfn name 'JB2'

; block zone
block zone generate edgelength 0.2

model save 'Geometry.dat'
```

11.2.4 Assign properties, equilibrate and load the pillar

```
model restore 'Geometry.dat'

model large-strain off

program call '00_Parameters.dat'
[paramS1_Mean] ;or any other of the defined parameters

; block constitutive model and properties
block zone cmodel assign elastic
block zone prop dens [dens] young [young] poisson [poisson]
block prop dens [dens]


; joint constitutive model and properties
block contact jmodel assign mohr

block contact property stiffness-normal [young] stiffness-shear [young] friction [friction] cohesion
    [cohesion] tension [tension]

block contact property stiffness-shear [stiffness_shear_B] stiffness-normal [stiffness_normal_B]
    friction [frictionB] cohesion 1e30 tension 1e30 range joint-set 2

block contact jmodel assign mohr range dfn-3dec 'JS1'
block contact prop stiffness-shear [stiffness_shear_S1] stiffness-normal [stiffness_normal_S1]
    friction [frictionS1] cohesion 1e30 tension 1e30 range dfn-3dec 'JS1'
;block contact property-distribution friction [frictionS1] deviation-uniform [frictionS1STD] range
    dfn-3dec 'JS1'

block contact jmodel assign mohr range dfn-3dec 'JS2'
block contact prop stiffness-shear [stiffness_shear_S2] stiffness-normal [stiffness_normal_S2]
    friction [frictionS2] cohesion 1e30 tension 1e30 range dfn-3dec 'JS2'
;block contact property-distribution friction [frictionS2] deviation-uniform [frictionS2STD] range
    dfn-3dec 'JS2'

;block contact jmodel assign mohr range dfn-3dec 'JB1'
;block contact prop stiffness-shear [stiffness_shear_B1] stiffness-normal [stiffness_normal_B1]
    friction [frictionB1] cohesion 1e30 tension 1e30 range dfn-3dec 'JB1'
;;block contact property-distribution friction [frictionB1] deviation-uniform [frictionB1STD] range
    dfn-3dec 'JB1'
;
;block contact jmodel assign mohr range dfn-3dec 'JB2'
;block contact prop stiffness-shear [stiffness_shear_B2] stiffness-normal [stiffness_normal_B2]
    friction [frictionB2] cohesion 1e30 tension 1e30 range dfn-3dec 'JB2'
;;block contact property-distribution friction [frictionB2] deviation-uniform [frictionB2STD] range
    dfn-3dec 'JB2'

block contact material-table default prop stiffness-shear [stiffness_shear_S1] stiffness-normal
    [stiffness_normal_S1] friction [frictionS1] cohesion 0 tension 0


; gravity
model gravity = 0, 0, -9.81

; boundary conditions
block gridpoint apply velocity-x 0 velocity-y 0 velocity-z 0 range position-z [brickz1]
block gridpoint apply velocity-x 0 range position-x [brickx1]
block gridpoint apply velocity-x 0 range position-x [brickx2]
block gridpoint apply velocity-y 0 range position-y [bricky1]
block gridpoint apply velocity-y 0 range position-y [bricky2]

; apply damping
block mechanical damping global

; group blocks
block gridpoint group 'top' range pos-z [brickz4]
block gridpoint group 'bottom' range pos-z [brickz1]

; equilibrate with high values of joint cohesion and tension
model solve
```

```
59
60  ; assign the realistic joint cohesion and tension
61  block contact prop cohesion [cohesionB] tension [tensionB] range joint-set 2
62  block contact prop cohesion [cohesionS1] tension [tensionS1] range dfn-3dec 'JS1'
63  block contact prop cohesion [cohesionS2] tension [tensionS2] range dfn-3dec 'JS2'
64  ;block contact prop cohesion [cohesionB1] tension [tensionB1] range dfn-3dec 'JB1'
65  ;block contact prop cohesion [cohesionB2] tension [tensionB2] range dfn-3dec 'JB2'
66
67  block mechanical damping combined
68
69  [global area = pillarW^2]
70  [global length = 1.5*pillarH]
71
72  fish def zzstress
73    ; compression positive, units MPa
74    local top_reaction = 0.0
75    loop foreach gp block.gp.list
76      if block.gp.group(gp) = 'top'
77        top_reaction = top_reaction - block.gp.force.reaction.z(gp)
78        local top_disp = block.gp.disp.z(gp)
79      endif
80    end_loop
81
82    zzstress = 1e-6*top_reaction/area
83    zzstrain = -1*top_disp/length
84  end
85
86  fish history zzstress
87  fish history zzstrain
88
89  ; define certain model
90  block history velocity-z position [pillarW] [pillarW] [brickz4]
91  model history mechanical ratio
92
93  fish def params_shear
94    global zvel_=-0.5
95  end
96  [params_shear]
97
98  [global cyc0 = mech.cycle]
99
100 ; velocity ramp with shape of CDF
101 fish def ramp
102   ramp = 1 / (1 + math.exp(-0.001 * ((mech.cycle - cyc0) - 10000)))
103 end
104
105 block gridpoint apply vel-z [zvel_] fish ramp range group 'top'
106
107 model cycle 20000
108
109 block gridpoint apply-remove vel-z range group 'top'
110
111 block gridpoint apply velocity-z [zvel_] range group 'top'
112
113 model cycle 300000
114
115 model save 'Pillar_Loading.dat'
```

11.3 Python solver to determine the pillar width

```
import numpy as np
import matplotlib.pyplot as plt
import sympy as sp

# Constants
UCS = 182                           # UCS
p = 2834                            # Density
DDF = 0.25                          # Discontinuity Dip Factor
FF = 1                              # Frequency Factor
LDF = 1 - DDF * FF                  # Large Discontinuity Factor
z = 150                             # Overburden
FoS = 2                             # Factor of Safety
X = 0.65 * UCS * LDF * 10**6        # Pillar strength equation
Y = p * 9.81 * z * FoS              # Overburden pressure
h = 7.5                             # Pillar height
R = 10

# Function and its derivative
def f(P):
    return (X * P**0.3) / (Y * h**0.59) - R**2 / P**2 - 2 * R / P

def f_prime(P):
    return (0.3 * X * P**(-0.7)) / (Y * h**0.59) + 2 * R / P**2 + 2 * R / P**2

# Initial guess
P = 1

# Tolerance level
tolerance = 1e-6

# Lists to store iteration values
P_values = [P]
iteration = 0

# Iterate using Newton-Raphson method
while True:
    P_new = P - f(P) / f_prime(P)
    P_values.append(P_new)
    iteration += 1
    if abs(P_new - P) < tolerance:
        break
    P = P_new


print("The pillar width is approximately:", P_new)

Width_Height = P_new/h

print("Width to height ratio:", Width_Height)
```